Generation, Detection and Optimisation of High order Harmonics in Neon

Jessica Dahlström

Abstract

In this thesis, high-order harmonics of an intense laser field were generated, detected and optimised. A spectrometer design was investigated in detail through ray tracing computer simulations. Mechanical and optical modifications were done to improve its performance and experiments in both argon and neon were performed. The experimental spectra reached the 100 eV range and showed a variation in shape and spectral range depending on the laser intensity. Calculations of single atom phase and phase matching were carried out to interpret the experimental results. In particular phase matching effects were found to be strongly intensity dependent and to have a significant effect on the spectrum shape and range.

Populärvetenskaplig sammanfattning

Då en intensiv ljuspuls växelverkar med materia kan ljuspulser av kortare våglängd sändas ut, så kallade övertoner. Dessa övertoner kan genereras i en ädelgas genom att en kort laserpuls, i detta fall 35 fs, joniserar atomerna. När de lösgjorda elektronerna återförenas med jonerna frigörs energi i form av ljus. Olika gaser är olika lätta att jonisera vilket gör att olika höga övertoner kan genereras. I de experiment som utförs här används inledningsvis argon där upp till 33:e övertonen genereras och sedan neon som med sin högre jonisationspotential kan ge betydligt högre överoner. Ett av målen med experimenten är att generera upp till 65:e övertonen i neon.
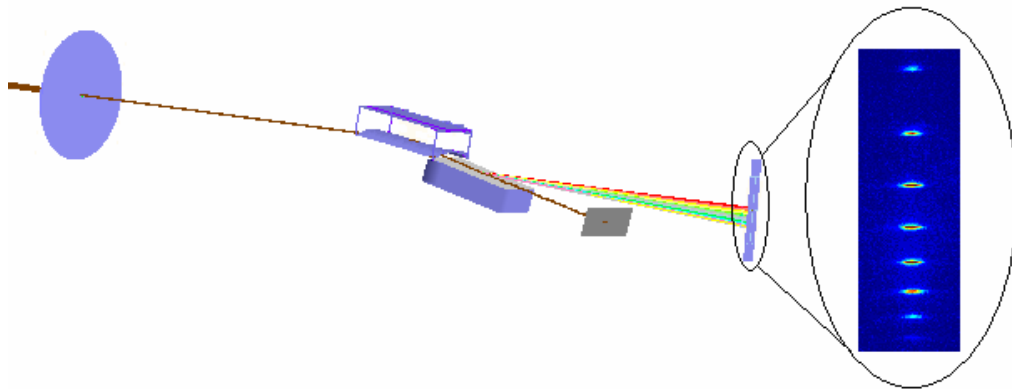
Övertonerna detekteras med en typ av spektrometer som inom ett visst intervall fokuserar alla våglängder i samma plan. Spektrometerns optiska design, dess ingående komponenter och systemets spektrala upplösning studeras med hjälp av ett datorprogram, FRED. Speciell vikt läggs vid det speciella gittret med varierande linjeavstånd och dess ljusfokuserande egenskaper. Även systemets avbildningsegenskaper och hur felaktig linjering påverkar dessa studeras. Med hjälp av resultaten från datorsimuleringarna modifieras sedan spektrometern både optiskt och mekaniskt så att den bättre kan detektera de höga övertonerna i neon.

Under experimenten testas först den modifierade spektrometern med argon som medium innan gasen byts ut till neon. Som bäst uppnås nu en signal innehållande upp till den 75:e övertonen, vilket mer än väl uppfyller målet. Ett annat intressant resultat är att även fasmatchningseffekter kan studeras genom att ändra laserns intensitet i mediet via en justerbar iris. Det visar sig att olika delar av spektrumet förstärks olika mycket vid olika intensitet, låg intensitet förstärker lägre övertoner vilka försvinner vid högre intensitet då istället högre övertoner förstärks.

De experimentella resultaten behöver nu tolkas med en teoretisk modell och detta görs med fasmatchningsberäkningar i en dimension. Modellen gäller då mediet är mycket längre än absorptionslängden. Utöver absorption tas hänsyn till dispersion, andel fria elektroner och polarisationens fasvariation i mediet. Beräkningarna visar att då mediet placeras före den genererande laserstrålens fokus ger låg intensitet fasmatchning av höga övertoner medan högre intensitet resulterar i fasmatchning av låga övertoner. Placeras mediet efter fokus gäller det omvända vilket överensstämmer med de experimentella

resultaten. En annan observation är att för fasmatchning av en viss överton krävs högre intensitet vid placering av mediet efter fokus än före, och dessutom krävs högre intensitet ju längre efter fokus mediet är placerat. Vid jämförelse med kvantmekaniskt beräknade övertonsspektra kan man se att de låga intensiteter som ger fasmatchning före fokus inte kan generera motsvarande övertoner medan överensstämmelsen är mycket bättre för de intensiteter som gäller efter fokus. Detta tyder på att fasmatchning är den viktigaste faktorn för att beskriva det fenomen som observerats vid experimenten. Den modell som använts är dock mycket enkel och behöver vidareutvecklas för att säkert fastställa att dessa slutsatser är riktiga.

Contents

1   Introduction

1.1 High order Harmonic Generation (HHG)

When a short laser pulse of high intensity interacts with matter the electric field of the light affects the atoms in the material. The nucleus and the electrons of an atom will be pulled in opposite directions creating a dipole moment which increases with the field strength. The polarisation depends on this individual dipole moment as well as on the number density of dipole moments. When the electric field is small this relation is linear while strong fields introduce nonlinear polarisation in the material. One interesting effect of this is the generation of higher frequencies, harmonics, of the driving field, illustrated by second harmonic generation in figure 1.1 (based on [1]). The harmonic wavelengths are in the XUV range, 121-10 nm, and short light pulses are generated, a few femtoseconds or even attoseconds in length, which are of interest for various applications such as research dealing with very fast processes, for example chemical reactions. In noble gases only odd harmonics can be emitted due to inversion symmetry. How high orders one can generate depends on the laser intensity as well as on the ionisation energy of the gas. For example neon has much higher ionisation energy than argon and thus higher harmonics can be generated. Another important parameter is phase matching. The larger the region is where the generating and the harmonic beams are in phase, the better the signal will be.
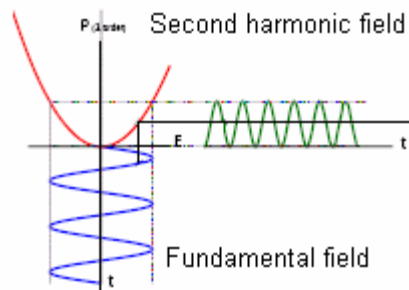

Figure 1.1: The incoming fundamental field creates a second harmonic field with the double frequency.

1.2 XUV Flat Field Spectrometer

In our experimental set up the HHG signal is examined using an XUV flat field spectrometer. A spectrometer separates light of many frequencies into a spectrum showing the different components. The optics generally consists of a set of concave mirrors or lenses focusing the light and a grating, often mirrors are used to avoid chromatic aberration. Different wavelengths are diffracted in different angles and if the focal length is not wavelength dependent this results in a curved focal plane. Using a CCD or other array type detector means that the detector plane is flat so that a curved focal plane results in aberrations such as astigmatism. The XUV flat field spectrometer used in this project utilises a toroidal mirror and a plane grating with varied line-space to correct these aberrations, see figure 1.2.
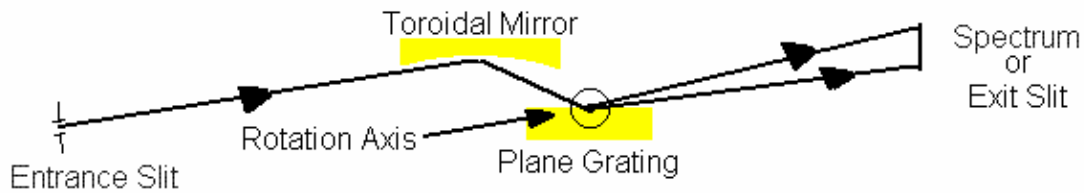
Figure 1.2: Optical layout of the XUV flat field spectrometer.

The spectrometer design is investigated and simulated in a modern ray tracing program, FRED, where characteristics like grating parameters, focus for different wavelengths and system resolution are studied.

1.3 Aim of thesis

The aim of this thesis is:

1. Improve the existing spectrometer to make it more suitable for detecting high order harmonics in neon. First FRED simulations are performed and with guidance by these results a new aluminium plate blocking the fundamental field is designed and the spectrometer optics is changed.

2. Experimentally generate high order harmonics in neon reaching the 100 eV range and examine the signal with the improved spectrometer.

3. Theoretically interpret the experimental results obtained, and in particular distinguish between single atom and phase matching effects.

1.4 Outline

The outline will follow this structure: Chapter 2 gives a description of the spectrometer studied in this project and its optical components followed by computer simulations for investigation of the optical design. The modifications done to the spectrometer are also presented. Chapter 3 presents the method and results of the performed experiments in argon and neon. In chapter 4 the theory of HHG and phase matching are presented together with some calculations as well as comparison with experiment. Chapter 5 contains a summary and outlook.

2 XUV Flat field Spectrometer

2.1 Description

2.1.1 Optical layout

The spectrometer in this project is an I.S.A. Jobin-Yvon PGM-PGS 200 XUV Monograph which can be used as a monochromator with an exit slit or a spectrograph without the exit slit. In this project the spectrometer mode is used. Figure 2.1 shows the optical layout.
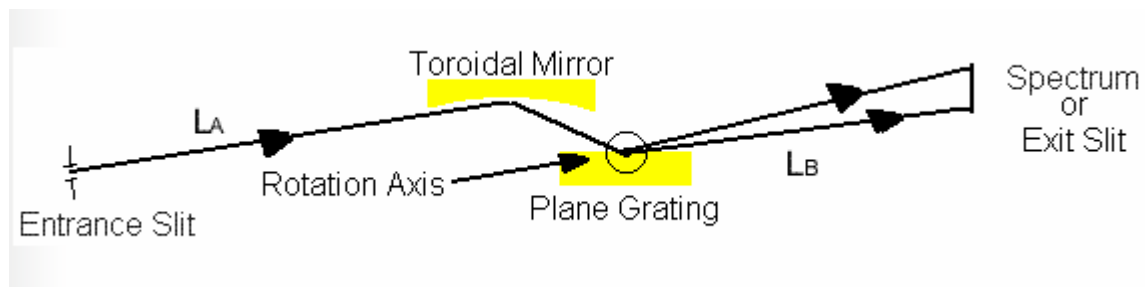

Figure 2.1: Optical layout of the XUV flat field spectrometer.

The light enters the spectrometer through the entrance slit, the toroidal mirror focuses the light and the plane, varied line-space (VLS) interference grating diffracts the light into a spectrum. The toroidal mirror together with the VLS grating produces a flat focal plane for a certain spectral range according to the grating properties. The lengths of the arms are L_A = 255 mm and L_B = 200 mm and the flat field spectrum is approximately 25 mm long. In monochromator mode the deviation angle is constant at 165 °. The width w of the entrance slit is continuously adjustable between 0 and 2000 μm but during experiments it is set to about 200 μm. Both the mirror and the grating have the dimensions 60×30×15 mm and the reflective surfaces are coated with gold. The choice of gold as coating is because the extreme ultra violet and soft x-ray wavelengths are strongly absorbed by most other materials. The refractive index of gold in this wavelength region is smaller than 1, resulting in total external reflection when used in grazing incidence. At the end of the exit arm the signal is detected by a microchannel plate (MCP). The MCP consists of a plate with an array of approximately 10 μm wide, parallel channels slightly tilted with respect to the plate surface. Every channel is an electron multiplier which results in amplification of the signal. Behind the plate a phosphor screen is placed for visualisation of the signal. When the electrons from the channels hit the screen visible phosphorescent light is emitted [2].

2.1.2 The toroidal mirror

The toroidal mirror has two different radii of curvature, one in the horizontal zx-plane and one in the vertical yz-plane. The radii of curvature are R_v = 1999.9 mm in the vertical (dispersion) plane and R_h = 32.48 mm in the horizontal plane. The relations between the

radii of curvature and the object and image distances are described by equation 2.1 and 2.2 in the vertical and horizontal case respectively [3]. The object distance is denoted r_o and the image distance r_i with an additional v or h for the respective case and θ is the angle of incidence.

$$\frac{2}{R_v \cos\theta} = \frac{1}{r_{o,v}} + \frac{1}{r_{i,v}} \tag{2.1}$$

$$\frac{2\cos\theta}{R_h} = \frac{1}{r_{o,h}} + \frac{1}{r_{i,h}} \tag{2.2}$$

With $r_o = L_A = 255$ mm plugged into these two equations both image distances are found to be in the same plane as the spectrometer flat field.

2.1.3 The varied line-space gratings

The grating in the spectrometer is a plane, varied line-space (VLS), interference grating. This means that the groove density varies from one end of the grating to the other, see figure 2.2. Varying the groove spacing across the surface of the grating moves the vertical focal curve, while keeping the grooves straight and parallel keeps the horizontal focal curve fixed [4].
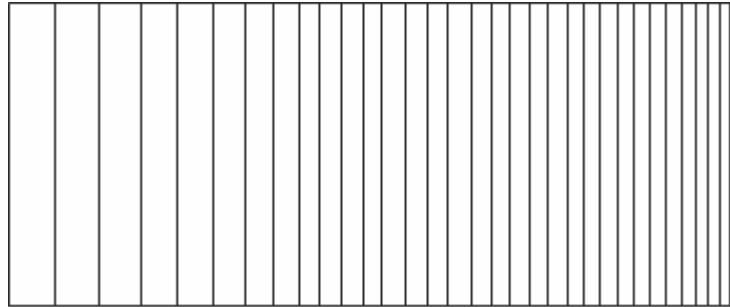

Figure 2.2: Varied line-space grating.

An interference (sometimes called holographic) grating is produced letting two light sources interfere producing a pattern on a substrate with a light sensitive surface. During exposure the interference fringes are transferred to the surface, then the substrate is immersed in a developing agent and a relief fringe pattern is formed. This method produces a sinusoidal groove profile in contrast to ruled gratings which usually have a triangular profile. The groove profile is important for the grating efficiency [4].

The angular dispersion D increases with the groove density G, the spectral order m and the diffraction angle β according to equation 2.3 [4]. This explains the focusing properties of the VLS grating.

10

$$D = Gm\sec\beta \qquad\qquad (2.3)$$

The spectrometer can be equipped with three different plane gratings with varied line-space according to table 2.1. According to the manufacturer the maximum grating efficiency is approximately 35 % for gratings with $\lambda/G < 0.2$ which is the case for all three gratings.

Table 2.1: Specified spectral ranges for the three gratings.

Grating	Grooves/mm	Spectral range [nm]	Energy [eV]
1	450	16-80	77-15
2	800	10-40	124-31
3	1800	4-20	310-62

Test results from the manufacturer specify the angles of incidence, α, and diffraction, β, for the central wavelengths for grating 1 and 3 and also the spectrum length, see table 2.2.

Table 2.2: Angles of incidence and diffraction for the central wavelengths of grating 1 and 3.

Grating	Wavelength [nm]	α [°]	β [°]	Spectrum length [mm]
1	50	87.444	77.556	25.3405
3	12	87.246	77.754	25.2403

2.2 FRED simulation

To get a better understanding of how the XUV flat-field spectrometer works and examine its properties a ray tracing program, FRED 7.70.0 from Photon Engineering, is used. The optical setup is constructed according to drawings and specifications from Jobin-Yvon.

The source of the HHG is modelled as a point source with an angular spread of 1 mrad (0.0573º). A 6 mm long and 0.1-0.4 mm wide entrance slit is placed at the global origin, 1500 mm from the point source. The detector is located 507.95 mm from the entrance slit. Grating 1 and 3 are designed to agree with test results from Jobin-Yvon. Such data were not available for grating 2 why this design is also based on the data for the other two gratings. The optical design of the spectrometer is displayed in figure 2.3.
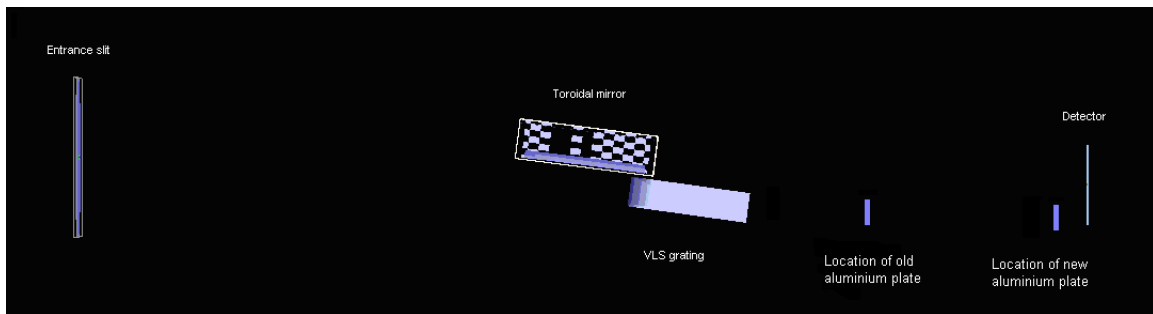

Figure 2.3: Optical set up for the flat field spectrometer.

2.2.1 Grating 1: 450 g/mm

First the difference between an ordinary grating with evenly spaced, straight grooves and a VLS grating is examined. For easier visualisation the larger width, $w = 0.4$ mm, is used for the entrance slit. As can be seen in figure 2.4 the ordinary grating scarcely focuses the light.
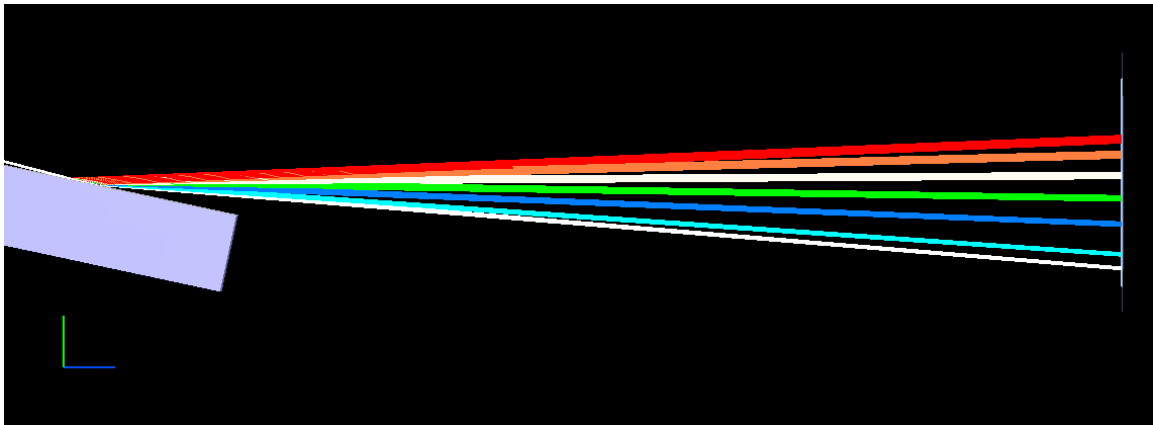

Figure 2.4: Grating with evenly spaced, straight grooves, 450 g/mm.

The positions spot diagram in figure 2.5 shows the image in the detector plane. The spectrum includes the longest wavelength (the topmost red maximum, 80 nm) and the shortest wavelength (the bottom white maximum, 16 nm) in the spectral range specified

for grating 1, as well as a few wavelengths in between. The maxima are rather wide and the width is changing rapidly with wavelength resulting in much narrower maxima for shorter wavelengths than for longer wavelengths. The maxima are also curved with the ends bent upwards. The length of the spectrum is approximately 24.8 mm.
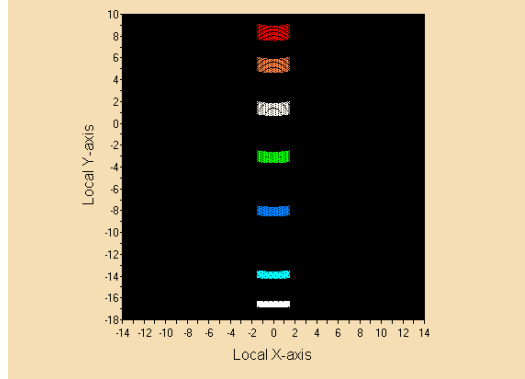

Figure 2.5: Positions spot diagram for the grating with evenly spaced, straight grooves, 450 g/mm.

A VLS holographic grating is created by clicking on the object surface and choosing "Two point exposure holographic optical element" under the "Grating" tab. For this grating the wavelength λ_{ref} = 500 nm is chosen for the two point sources creating the interference pattern for the grooves. The phase departure attribute is used to create varied line-space. With the XY polynomial choice a linear grating is made as follows: Equation 2.4 is the polynomial equation for the grating spacing *d(z)* and equation 2.5 is the corresponding phase function *f(z)* in FRED.

$$d(z) = \frac{\lambda_{ref}}{a + 2bz + 3cz^2 + ...} \tag{2.4}$$

$$f(z) = az + 2bz^2 + 3cz^3 + ... \tag{2.5}$$

For a linear change in line-spacing a polynomial with two variables is needed. Inserting $d(-30) = 280$ g/mm and $d(30) = 620$ g/mm in equation 2.4 two equations are obtained. Solving these equations simultaneously gives $a = 0.225$ and $b = 1.4167 \cdot 10^{-3}$. In FRED the variables *a* and *b* corresponds to the coefficients X0Y1 and X0Y2. The diffraction order is set to -1 for wavelengths within the spectral range of the grating. With these settings the vertical focus of the central wavelength is located at z = 458.75 mm, about 50 mm in front of the detector, see figure 2.6. The focus of the zero order beam is located at z = 394 mm. The magnification M of the system is $M = 1.054$ for the central wavelength, this is close to 1 as the spectrometer is designed for. Figure 2.7 shows a positions spot diagram of the resulting spectrum for this grating including the same wavelengths as before and obviously the maxima are now narrower with a more uniform width than in figure 2.5. It is also worth noticing that the ends now are bent downwards, opposite to what they were before.
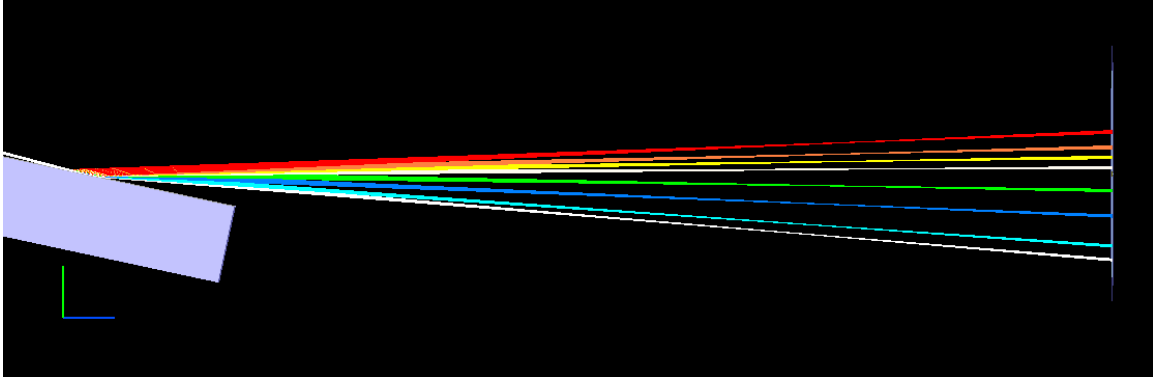
Figure 2.6: Grating with varied line-space, straight grooves, 450 g/mm in the centre.
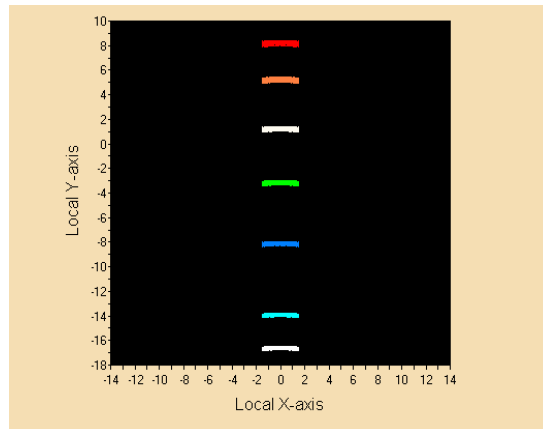

Figure 2.7: Positions spot diagram for the grating with varied line-space, straight grooves, 450 g/mm in the centre. The focus is located between the grating and the detector.

A similar simulation is also performed for a grating with the focus located after the detector but still with $M \approx 1$. The settings in this case are $a = 0.225$ and $b = 6.667 \cdot 10^{-4}$ corresponding to $d(-30) = 370$ g/mm and $d(30) = 530$ g/mm, the magnification $M = 1.08$. The focus of the central wavelength is now at z = 551.25 mm, roughly 43 mm behind the detector, and for the zero order the focus is found at z = 390 mm, 118 mm in front of the detector. The resulting positions spot diagram is shown in figure 2.8 containing the same wavelength range as figure 2.5 and 2.7, now the ends are bent slightly upwards. This implies that the curvature of the maxima changes at the focus, from a U-form before the focus via a straight line at the focus to a U turned upside down after the focus. This is also easily understood by thinking about the position of the rays in the beam. The rays situated in the lower part of the beam before the focus will be crossing the rays from the upper part of the beam at the focus and thereby end up changing place with them after the focus leading to an image turned upside down.
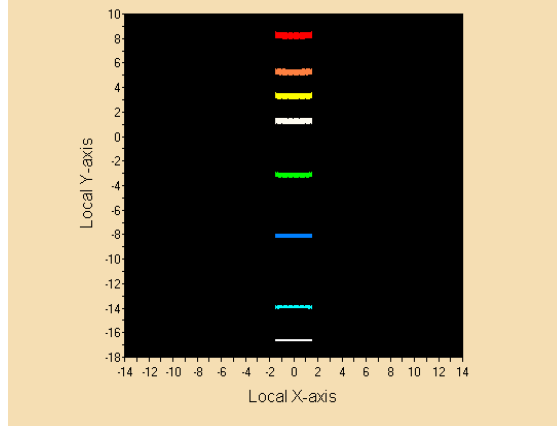
14

Figure 2.8: Positions spot diagram for a VLS grating focusing after the detector.

Since the interest of this thesis is optimising the spectrometer for looking at harmonics a simulation is performed for the harmonic orders 16-31. The simulation is performed for the grating focusing before the detector because of the similarity of the curvature of the maxima to experimental results. Here the width of the slit is set to 100 μm.
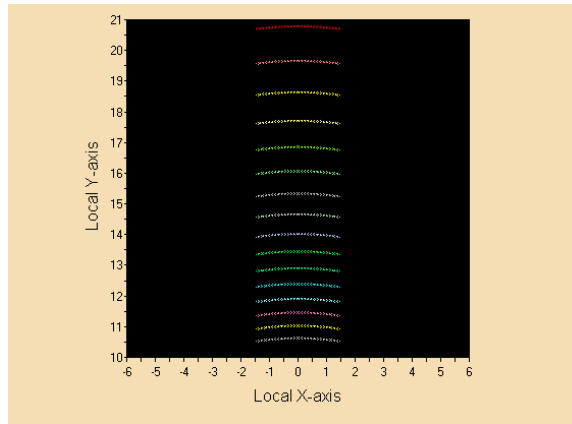

Figure 2.9: Harmonic orders 16-31, odd and even, with the 450 g/mm
VLS grating focusing 50 mm before the detector.

2.2.2 Grating 2: 800 g/mm

A VLS grating with 800 g/mm is created as described before, but with the phase departure coefficients $a = 0.4$ and $b = 2.58333 \cdot 10^{-3}$. The corresponding line-spacing is $d(-30) = 490$ g/mm and $d(30) = 1110$ g/mm giving a magnification $M = 1.024$. The spectrum length is now measured to 24.63 mm. With these settings the focus of the harmonic beam ends up before the detector at z = 466 mm. The zero order beam is focused at z = 390 mm.

2.2.3 Grating 3: 1800 g/mm

The VLS grating with 1800 g/mm is created with phase departure coefficients $a = 0.9$ and $b = 2.5 \cdot 10^{-3}$. The corresponding line-spacing is $d(-30) = 1500$ g/mm and

$d(30) = 2100$ g/mm and the magnification $M = 0.96$. In this case the spectrum length is 25.22 mm and the focus of the harmonics is now located after the detector at z = 612 mm, the focus of the fundamental beam is located at z = 390 mm. A simulation of harmonics orders 88-114, both odd and even orders, is performed shown in figure 2.10.
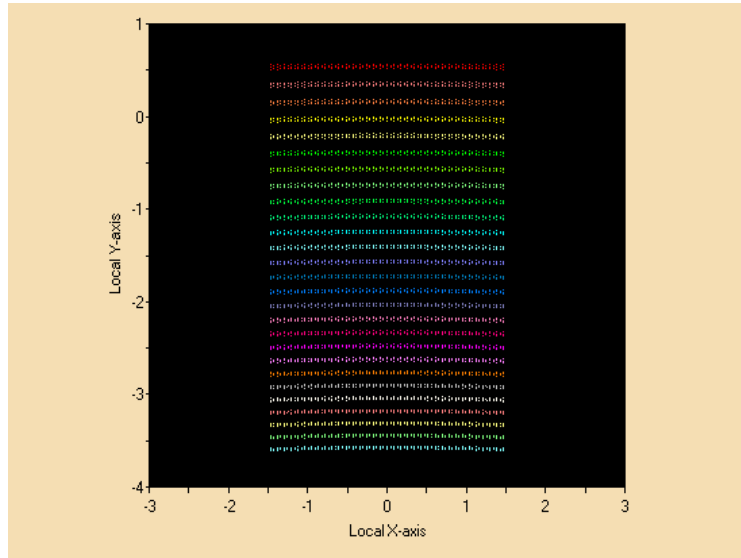

Figure 2.10: Simulation of harmonic orders 88-114, odd and even,
with the 1800 g/mm VLS grating.

Figure 2.11 shows a comparison between the grating with 450 g/mm and the one with 800 g/mm. Harmonic orders 16-31 were simulated and from the scale on the y-axis it is obvious that the spectrum from the grating with 800 g/mm is more stretched out (due to higher dispersion) than the other one, about 16 mm compared to 11 mm.
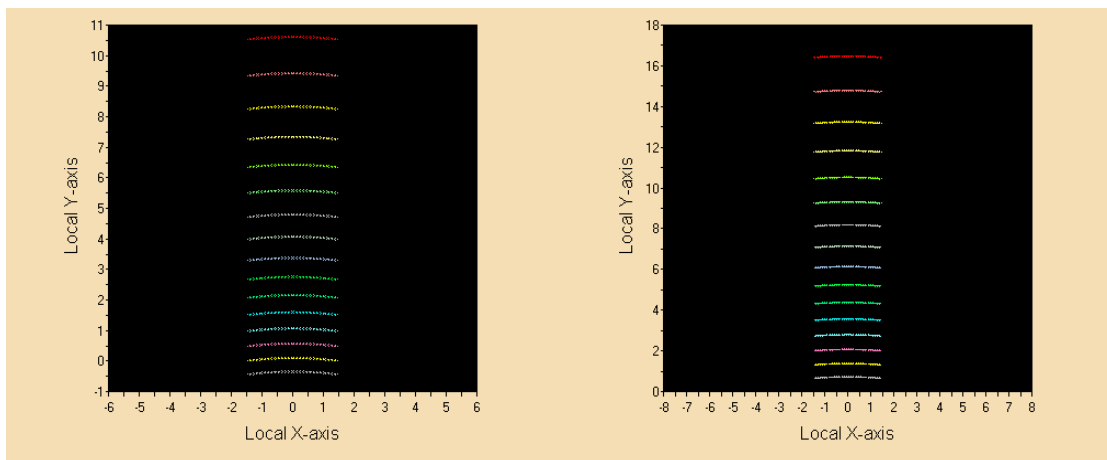

Figure 2.11: Harmonic orders 16-31, both odd and even, with the 450 g/mm grating (*left*)
and the 800 g/mm grating (*right*).

Figure 2.12 shows the position of the detector, the fundamental focus and the focus of the central wavelength for the different VLS gratings denoted G1, G2 and G3. On the horizontal axis the longitudinal distance from the entrance slit is shown and the vertical axis shows the vertical distance from the centre of the entrance slit.
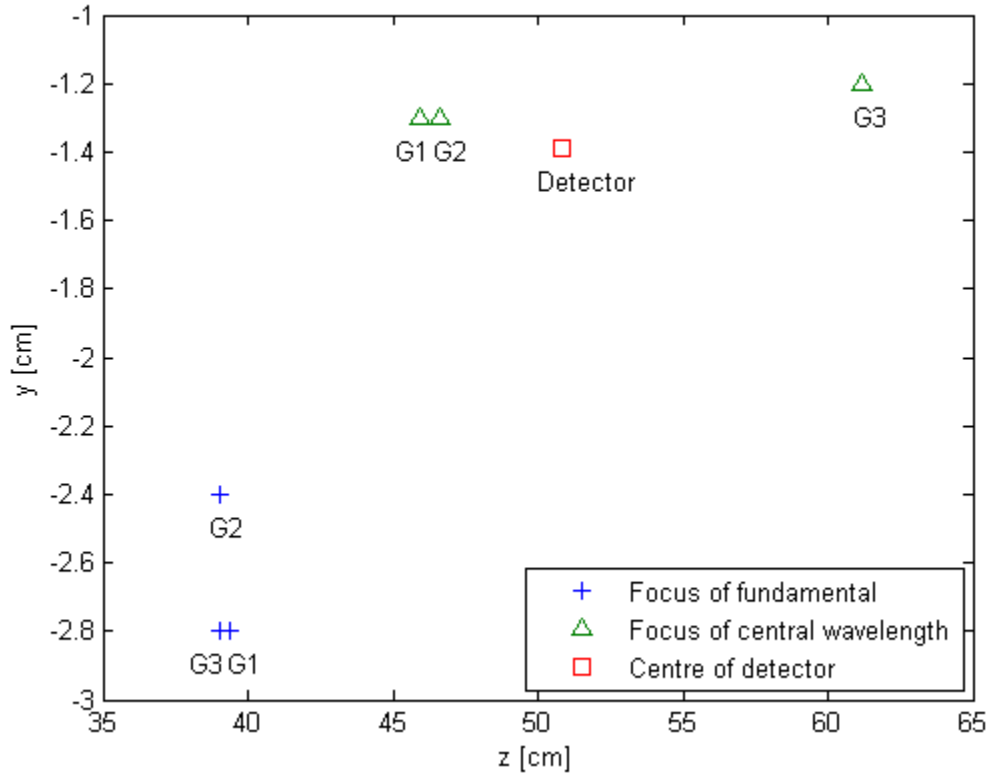

Figure 2.12: Longitudinal and vertical distance from the entrance slit to the detector, the fundamental focus and the focus of the central wavelength for the different VLS gratings: G1, G2 and G3.

2.2.4 Resolution

The possibility to move the detector from the current place to the focus of the harmonic beam is discussed. It is decided that for this existing spectrometer it would be complicated to block the fundamental far enough from the fundamental focus to prevent creating plasma without blocking the harmonics. Still it is interesting to see how such a modification would affect the system resolution. The resolution is examined for the different gratings 1, 2 and 3 and the slit width is set to 0.1 mm. For all gratings the analysis is performed at the original detector place, 507.95 mm from the slit as well as at the focus of the central wavelength. The resolving power R is a measure on the ability to resolve two adjacent spectral lines of average wavelength λ, usually expressed as a dimensionless quantity as in equation 2.1 [4].

$$R = \frac{\lambda}{\Delta\lambda} \tag{2.1}$$

$\Delta\lambda$ is the difference in wavelength between two just distinguishable spectral lines, also called the limit of resolution or just resolution. The results for the three gratings are found in table 2.3.

Table 2.3: Resolution at detector and focus for the three gratings.

Grating	At the detector	At focus
1	$R = 156.75$	$R = 556.1$
	$\Delta\lambda = 0.32$ nm	$\Delta\lambda = 0.09$ nm
2	$R = 192.81$	$R = 833.83$
	$\Delta\lambda = 0.13$ nm	$\Delta\lambda = 0.03$ nm
3	$R = 185.12$	$R = 857.64$
	$\Delta\lambda = 0.065$ nm	$\Delta\lambda = 0.014$ nm

Before beginning the experiments simulations are made with grating 1, the grating that will be utilised in the initial experiments with argon, to check if the aluminium plate blocking the fundamental may also block the harmonics. According to simulations there is no risk of blocking the harmonics with the plate. The distance between the fundamental and order 32 is at least 15 mm in the detector plane when the fundamental is on the top edge of the plate. There should not be a risk with grating 2 that will be used in the neon experiments either, because it is optimised for higher orders which will then replace these lower orders in figure 2.13.
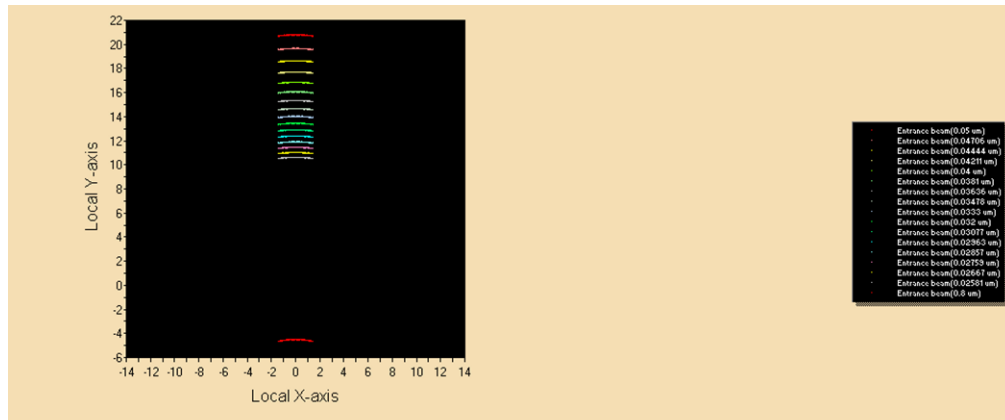

Figure 2.13: Simulation of fundamental and harmonics 16-32.

18

2.2.5 Alignment

Before replacing the old spectrometer optics simulations are performed to see how improper alignment would affect the image. The coordinate system referred to in the following sections is defined as in figure 2.14.
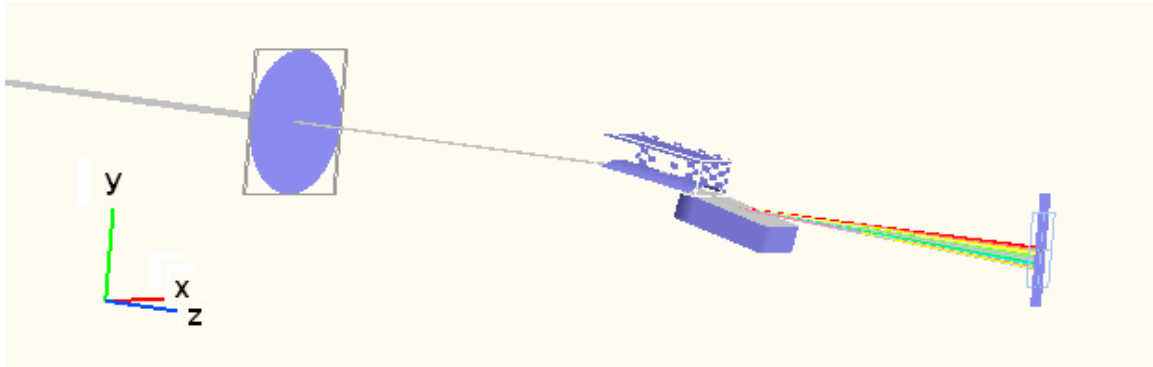
Figure 2.14: Coordinate system explaining the positions of the optical elements in the spectrometer.

Toroidal mirror

The first test is rotating the toroidal mirror in the xz-plane. The mirror is rotated around y +1° and -1 °. The result is that the fringes will be closer together on one side while diverging on the opposite side, see the left and right parts of figure 2.15. The spectrum length is not affected.

Figure 2.15: *Left:* Mirror rotated +1 degree about y. *Right:* Mirror rotated -1 degree about y.

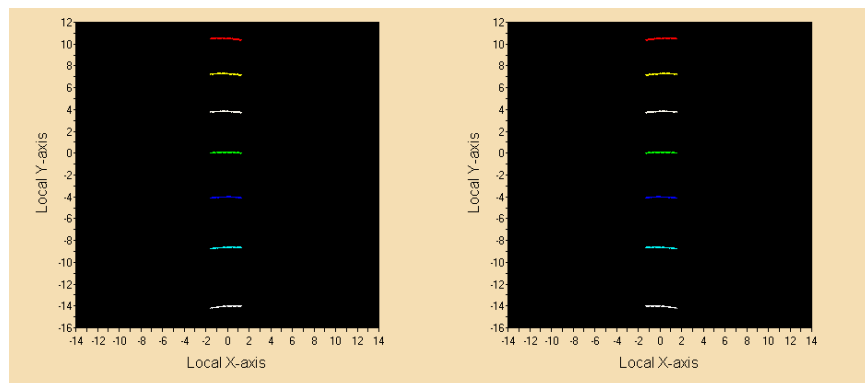Next the mirror is rotated in the xy-plane. Rotating it around z +2º or -2 º results in tilted fringes, one end is leaning downwards and the other slightly upwards, the spectrum length is still not affected. This is illustrated in figure 2.16, the left part shows +2º rotation and the right part shows a rotation of -2º around z.
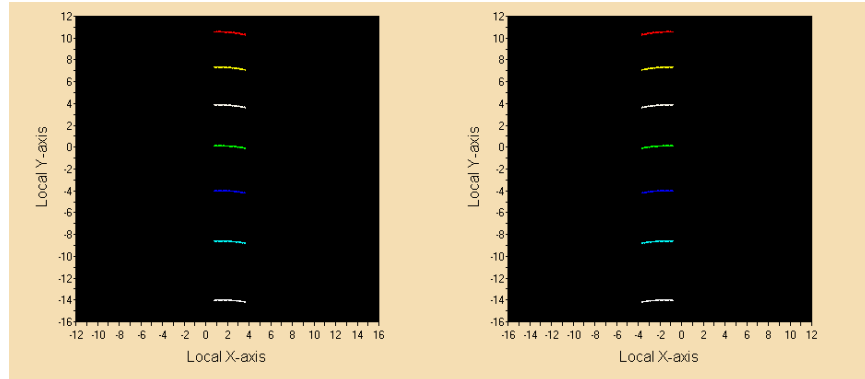

Figure 2.16: *Left:* Mirror rotated +2 degrees about z. *Right:* Mirror rotated -2 degrees about z.

When rotating the mirror in the yz-plane the magnification changes. +1º rotation around x to 8.32 º results in a wider image with reduced height, shown in the left part of figure 2.17, also the position of the central wavelength is slightly raised. -1º rotation to 6.32º makes the beam miss the grating, but -0.5º reduces the width while heightening the image as can be seen in the right part of figure 2.17. In this case the position of the central wavelength is slightly lowered.
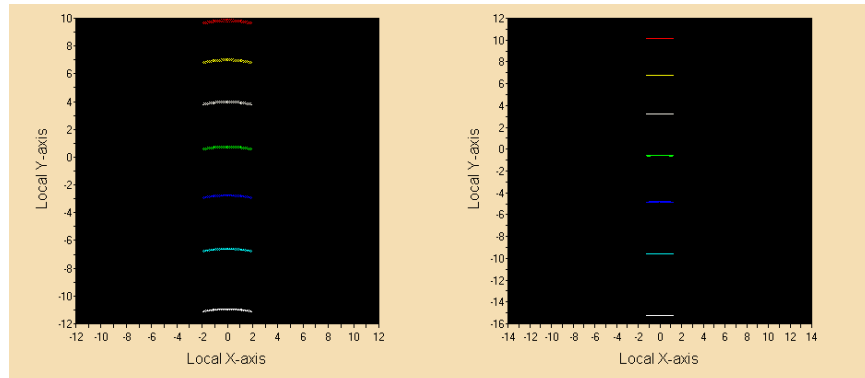
Figure 2.17: *Left:* Mirror rotated +1 degree about x. *Right:* Mirror rotated -0.5 degree about x.

Shifting the mirror in the x direction gives the same result as rotating it around z. A shift of +1 mm results in an image similar to the result of rotating the mirror +2º around z and a -1 mm shift gives a similar result as rotating -2º around z.

A slight shift in the positive y direction does not alter the image while a shift in the negative y direction lowers the image position.

Shifting the mirror in the positive z direction lowers the image position while the opposite is true for a shift in the negative z direction.

20

VLS grating
Rotating the VLS grating +1º around x lowers the image while a -1º rotation around x raises the image position slightly.

Rotating the grating +1º around y shifts the image slightly to the right, a rotation in the opposite direction results in a slight shift to the left.

Rotating the grating around z +1º shifts the image to the left as well as tilts the fringes as the right part of figure 2.16. A rotation of -1º results in a shift to the right and a tilt as in the left part of figure 2.16.

2.3 Improvement of the spectrometer

2.3.1 Eliminating the fundamental

The first spectrometer problem that needs to be dealt with is blocking the fundamental beam. The old blocking device is an aluminium plate which according to the previous computer simulations is placed close to the focus of fundamental, approximately 400 mm from the entrance slit. The intense laser beam destroys the filter creating plasma that is scattered onto the VLS grating, covering the reflective surface and causing deterioration of the performance. Instead of dispersing and focusing most of the light into the wanted signal a growing part of it is spread in all directions inside the spectrometer amplifying the background light. The signal gets weaker and might eventually disappear in the rising background. To get rid of this problem a new plate is designed which is placed in the far end of the exit arm of the spectrometer, just before the MCP. The position of the zero order beam is measured letting the beam of a 633 nm HeNe laser pass through the spectrometer. The plate is designed so that when the grating is rotated the position of the zero order will never exceed the top edge of the plate. Front and side view drawings of the plate are displayed in figures 2.18 and 2.19.
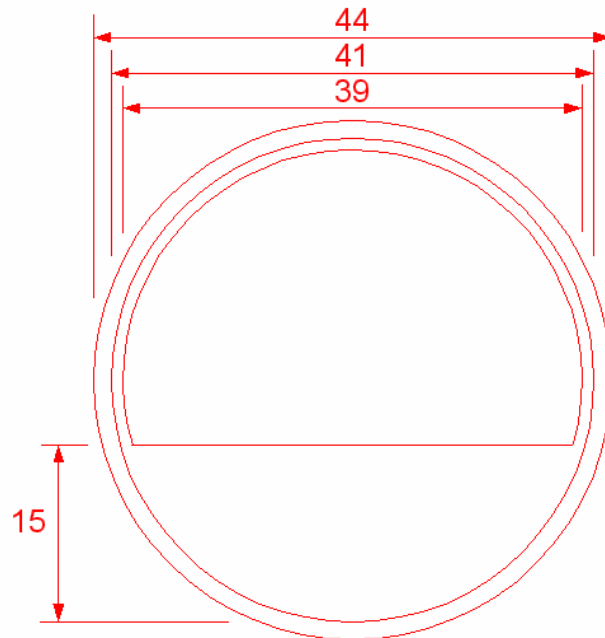

Figure 2.18: Front view of the aluminium plate blocking the fundamental.
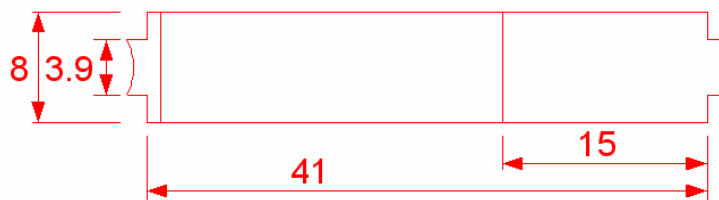
Figure 2.19: Side view of the aluminium plate blocking the fundamental.

2.3.2 Replacing optics and aligning the spectrometer

When replacing the spectrometer optics it is important to be very careful not to touch the reflective surfaces, they are easily damaged. Only the mirror mount needs to be removed completely from the spectrometer, this is easily done by removing the two screws fixing it to the cover. Mark the position of the old optics before removing them, this makes it easier to put the new optics in their correct positions. Mark the beam position carefully somewhere after the spectrometer before removing the old optics. Make sure the new optics have the same dimensions as the old ones before mounting them, if they are thicker there is a risk that they will touch resulting in destroyed reflective surfaces. There are two sets of holes for the screws to the mirror mount, the lower pair should be used for a thicker mirror and the upper pair for a thinner mirror. If the grating is to be replaced this must be done before reinstating the mirror mount. The grating is placed on the mount according to the pencil marks made before removing the old grating and fastened with the holder screws. The rotation of the mirror is controlled by screws on top of the mount making it possible to adjust after the mount is fastened to the cover.

When aligning the spectrometer it is mostly the mirror that can be adjusted, carefully turn the screws one by one, little by little to direct the beam to the previously made marks. Make sure the image shape is correct or the image will be distorted and the aberration correcting properties of the spectrometer will be destroyed.

3 Experiment method and results

3.1 Experimental setup

During experiments the Terawatt laser system at the Lund High Power Laser Facility is used for harmonic generation. It is a chirped pulse amplified Ti:Sapphire system at a wavelength of 800 nm. The beam width is about 5 cm and the pulse length after the compressor is about 35 fs. The High order Harmonic Generation setup is displayed in figure 3.1.
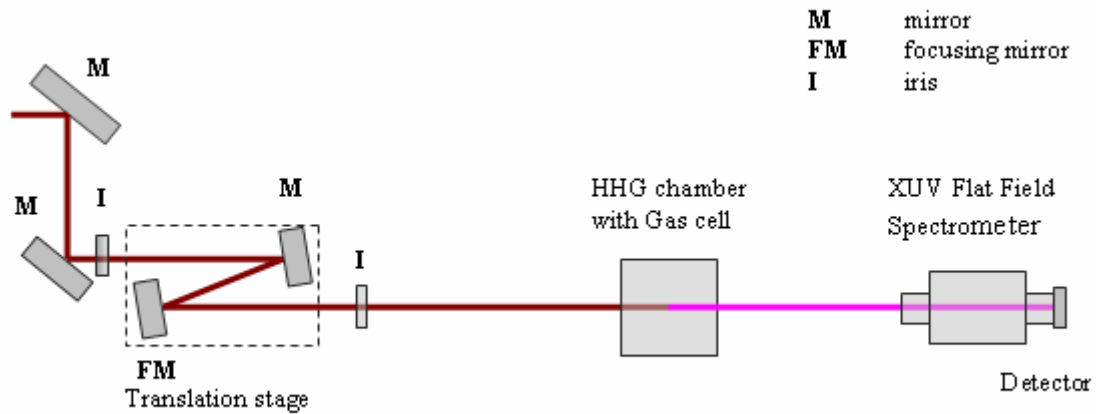
Figure 3.1: Experimental setup

The incoming laser beam is reflected by two mirrors before going through an iris with adjustable diameter. It is then reflected again by a mirror on the translation stage before it is focused by the focusing mirror with 2 m focal length. The beam then goes into a pipe through a glass window and the rest of the system (pipes, HHG chamber, spectrometer and detector) is in vacuum. In the HHG chamber the gas comes into the gas cell via a hole in the centre, synchronised with the laser pulses. The gas pressure in the cell is about 5 mbar. The harmonic beam is detected by the XUV flat field spectrometer described in chapter 3 and the signal is recorded by the detector, a micro-channel plate (phosphor screen). A CCD camera monitors the detector signal.

3.2 Argon experiments

The experiments can be divided into two parts: First the aim is to test the new fundamental blocker and replace the old destroyed optics with new optics, this also includes replacing grating 1 with grating 2. These experiments are performed with argon as the target gas. The aim of the second part of the experiments is changing the target gas to neon and record a spectrum reaching 100 eV, corresponding to harmonic order 65.

The new aluminium plate is installed and proven to block the zero order the way it was supposed to. The argon spectra recorded contain harmonic orders 17-31, and also show that the higher orders are far from the filter edge so there do not seem to be any risk of blocking them. To be on the safe side the spectrometer is opened and the filter is examined to make sure it is not damaged by the blocked laser beam. No marks are observed indicating that no plasma is created and the new optics can be safely installed.

When replacing the old optics it is discovered that the new toroidal mirror is thicker than the old one. Because of this a new pair of holes is drilled 3 mm below the original one in the mirror mount. Using the old pair of holes there is a risk of the new mirror touching the grating and destroying the surface of both of them. The spectrometer is then realigned and new experiments with argon are performed.

The recorded argon spectra now look stronger and sharper due to the reduced background light level. One example is shown in figure 3.2, it is difficult to see but the maxima are slightly curved like a U upside down indicating that the focus is located between the grating and the detector. Compared to spectra recorded earlier the curvature is now much smaller.
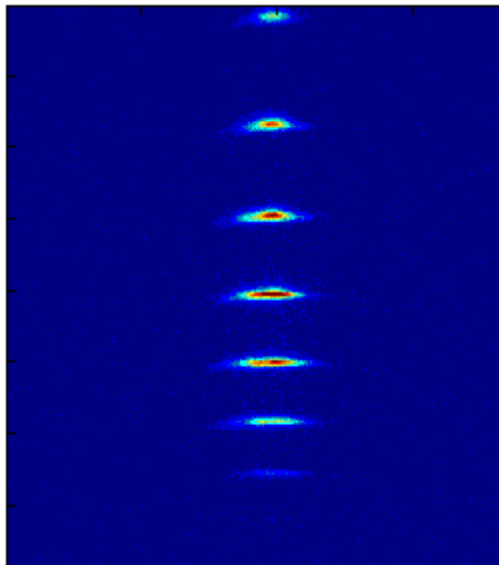

Figure 3.2: Nice looking spectrum in argon.

Unfortunately a new unexpected problem occurs, when tilting the grating to move the spectrum downwards the fundamental shows up again, now reflected in the pipe making up the spectrometer exit arm. A spectrum with the zero order reflection is shown in figure 3.3. Also it is clear that the lower orders of the signal are getting weaker, this is explained by the grating being optimised for shorter wavelengths so that the angle of incidence becomes too large when rotating the grating too much.
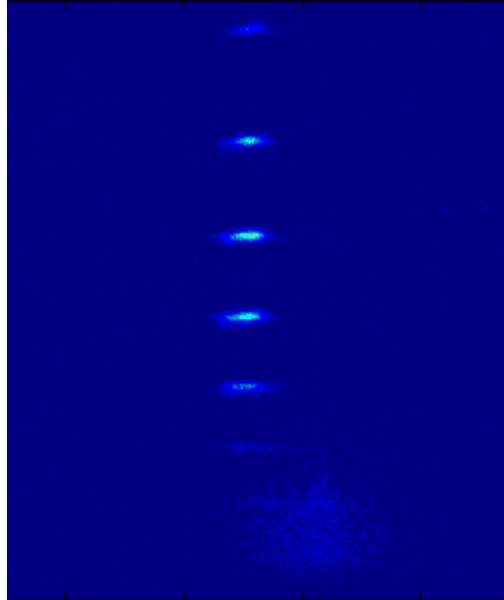

Figure 3.3: Spectrum in argon with zero order reflection.

3.3 Neon experiments

When changing the gas to neon it gets very difficult to get a signal. The neon spectrum should be approximately 2-3 orders in magnitude weaker than in argon because of the higher ionisation potential which impairs the efficiency of the HHG. Since the absorption length in neon is longer than in argon, a longer gas cell and high pressure is desirable in order to optimise phase matching.

In order to reach higher pressure in the gas cell the piezoelectric element opening the gas supply to the gas cell is adjusted. It is discovered that for argon the pressure got from 10^{-6} to 10^{-4} bar when letting the gas in but with neon it only reaches $4 \cdot 10^{-5}$ bar. Probably this is not the true value because the gauge measures gas ionisation, neon has a much higher ionisation potential than argon why less of it will be ionised and the pressure will appear to be lower even if that is not really the case.

Before continuing experiments the 23 mm long gas cell is carefully realigned and a spectrum in neon is finally obtained with the following settings: The laser energy is 140 mJ before the compressor and the gas pressure in the buffer is about 2.9 bar. Changing the position of the focus in the gas cell by altering the horizontal position of the gas cell is found to change the phase matching condition and different parts of the spectrum are observed. In one position the higher orders are the strongest while in another position lower orders are enhanced while higher orders get weaker. Orders 45-77 are visible.

The best results are obtained in an experiment with even higher laser energy, 170 mJ. The spectrum is found to be very sensitive to opening and closing the iris on the translation stage. Data are recorded for five different iris diameters, one smaller than 17 mm, 17 mm, 19 mm, 21 mm and 22 mm. A small iris diameter cutting a large part of the laser beam results in lower intensity in the focus and the lower energy part of the spectrum (lower orders) is observed. The more of the laser beam that is let through the iris, the further the observed harmonics are shifted towards higher energies and the signal gets weaker. One problem occurring is that when higher orders are observed the reflected fundamental shows up again making it more difficult to see the highest harmonics since the reflected light is stronger than the signal. Also the position of the focusing mirror is altered finding a more optimised position for the focus. In the beginning of the experiment the focus is somewhere before the gas cell, moving it closer to the centre of the gas cell the signal gets stronger and also a change in the spectral region is observed due to change in intensity. This change of the phase matching condition is easier to achieve by controlling the iris diameter. The results with the focus located before the gas cell are displayed in figure 3.4 and the results with the focus closer to the centre of the gas cell can be seen in figure 3.5.
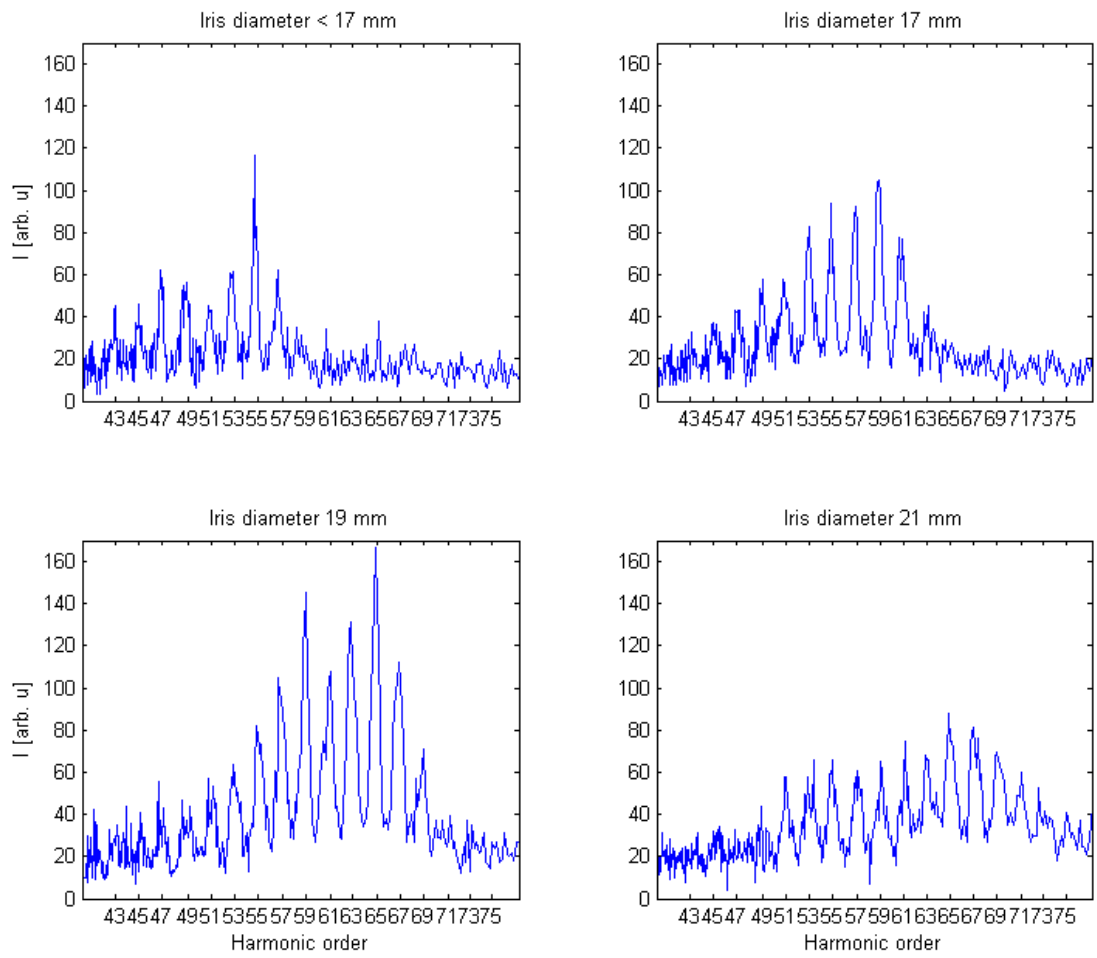
Figure 3.4: Changing the phase matching condition with the focus located
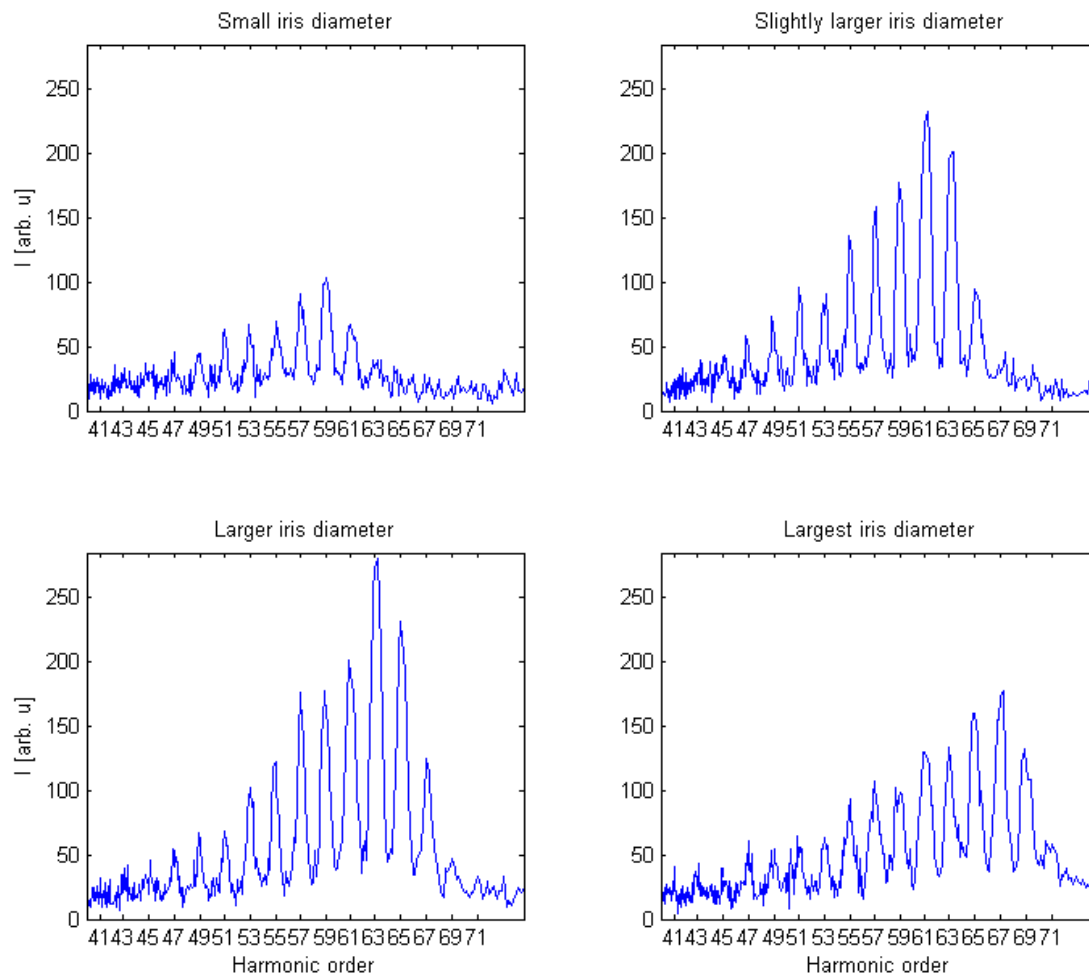a few cm before the centre of the gas cell.

28

Figure 3.5: Changing the phase matching condition with the focus centred in the gas cell, the best signal of all is obtained with the "Larger iris diameter".

4 Theory and discussion

4.1 Single atom response

4.1.1 Three step model

The key process behind the many interesting phenomena appearing during interactions between strong laser fields and atoms is ionisation. There are three different regimes in which ionisation can happen [5], see figure 4.1 [6]. The superposition of the electric field of the laser and the atomic Coulomb potential results in a deformed atomic potential changing with the time dependent applied field. At low and moderate laser intensities, the *perturbative regime*, the ionisation probability is small and absorption of multiple photons is needed for ionisation. In the *strong-field regime* the potential is so strongly suppressed by the laser field that the wave function of the most weakly bound electron may penetrate the barrier and the electron tunnels out into the continuum. In this regime high order harmonic generation can take place. At even higher field strengths the *relativistic regime* is reached where the atomic potential is suppressed below the energy of the most weakly bound electron,-Wb, which is released into the continuum via ionisation.
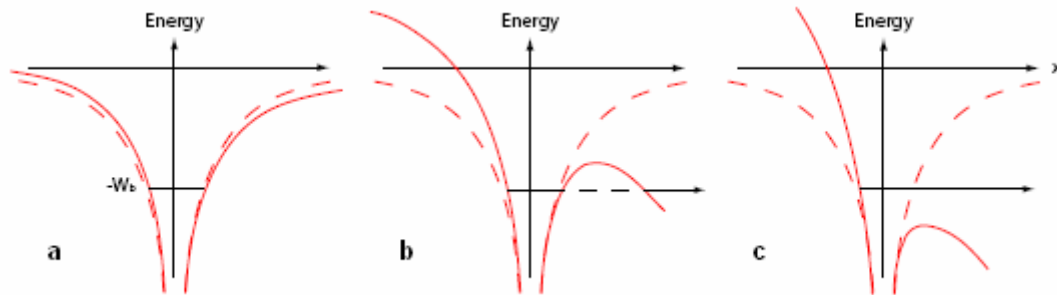
4.1: *a:* Multiphoton ionisation   *b:* Tunnelling ionisation   *c:* Over the barrier ionisation

The three step model is a semi-classical way of describing the physics of high order harmonic generation. Consider an electron in an atomic potential. When the atom is exposed to an intense laser field the potential is deformed by the oscillating electric field, see figure 4.2 [7]. The electron then experiences a lower barrier and thus its probability to tunnel out into the continuum increases (1). The free electron is accelerated away from the ion by the electric field (2) and when the field changes direction the electron is again driven back towards the ion core. It may then recombine with the atom and send out a photon (3).
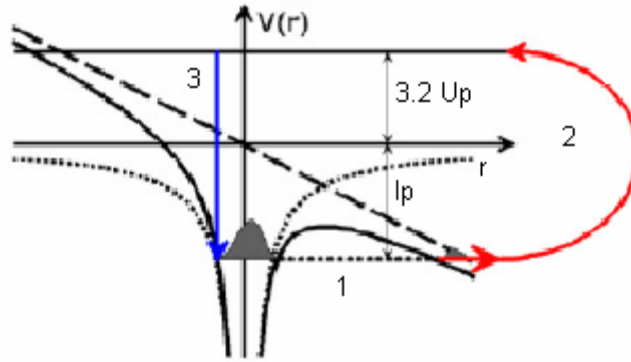
Figure 4.2: Schematic image of the three step model.

HHG can occur in linearly polarised laser light, but not in light with circular polarisation. This is easily understood by imagining the atom in a frame rotating simultaneously with the circularly polarised electric field. The laser field then seems to be constant resulting in a static response so that the only atomic response is at the laser frequency itself. In figure 4.3 [8] it is easy to see that an electron ionized before the peak of the electric field within the optical cycle will not return to its parent ion, while one ionised at the peak or in the following quarter period will recombine with the ion again. This process will repeat itself every half-cycle resulting in a spectrum of high order harmonics.

Figure 4.3: Recombination possibility at different times of ionisation.

The energy E_n of the emitted photon depends on the ionisation potential I_p of the atom and the kinetic energy E_k that the electron gained during acceleration in the electric field. The kinetic energy of the electron depends on when during the laser cycle the electron entered into the continuum and thereby the time it spent there. This also means that the electron will follow a shorter or longer trajectory outside the atom. Because of the anti symmetry of the driving electric field it is enough to study tunnelling times in the interval $t_t \in [0, T/2]$. The shortest electron trajectory corresponds to no time in the continuum while the longest trajectory stays approximately one period in the continuum before recombination, see top part of figure 4.4. The long trajectories are the result of ionisation in the part of the laser pulse where the electric field is close to its peak value while ionisation far from the peak where the electric field changes sign results in short trajectories. This influences the kinetic energy of the returning and thereby the energy of the emitted photon depends on the tunnelling time of the electron, see lower part of figure 4.4.
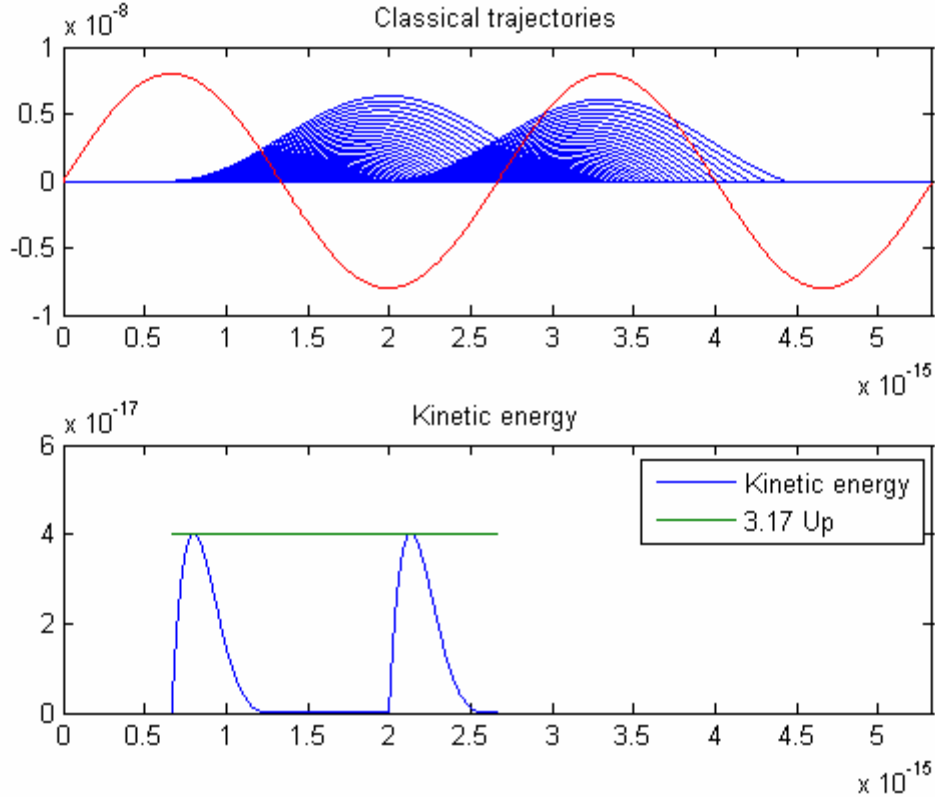
Figure 4.4: *Top:* Classical trajectories (blue) and laser E-field (red).
Bottom: Kinetic return energies of the electrons, maximum return energy corresponds to 3.17 Up.

Assuming the electron wave packet is only influenced by the electric field of the laser, ignoring the effect of the atomic potential and the magnetic field, the path it travels can be calculated classically. The electric field is described as $E(t) = E_0 \sin(\omega t)$. At time t_t the electron tunnels through the barrier and appears in the continuum with zero velocity. It is then assumed that the only force acting upon it can be described according to Newton's second law and the electrostatic force $F(t) = m\ddot{x} = eE(t)$. The expressions for velocity $v = \dot{x}(t)$ and position $x(t)$ are obtained by integration. The return time t_r for different tunneling times t_t is determined by numerical calculations and finding zero-crossings in $x(t)$. The return energy Er is then calculated according to equation 4.1.

$$E_r = \frac{mv^2}{2} = \frac{e^2 E_0^2}{2m\omega^2}(\cos(\omega t_r) - \cos(\omega t_t))^2 \tag{4.1}$$
$$= 2U_p(\cos(\omega t_r) - \cos(\omega t_t))^2$$

For the classical calculations of electron trajectories and single atom phases for HHG in neon in chapter 4.2.2 the following parameters are used: The laser intensity I_0 is in the interval $[2.0 \cdot 10^{18}, 1.0 \cdot 10^{19}]$ W/m^2, the wavelength of the generating beam is $\lambda_0 = 800$ nm and the ionisation potential $I_p = 21.6$ eV.

The bottom part of figure 4.4 shows that the electron return energies are

$$E_k \leq 3.17 \cdot U_p$$

U_p is the ponderomotive energy which is the average kinetic energy gained by a free electron in an E-field and is defined as follows:

$$U_p = \frac{e^2 E_0^2}{4m\omega_0^2}$$

According to this classical treatment the maximum energy of the emitted photon, the cut-off energy, is $I_p + 3.17 \cdot U_p$ where I_p is the ionisation potential of the atom, for neon this is 21.6 eV. Figure 4.5 shows the kinetic energy as a function of τ, the electron time of flight defined as the difference between the return time t_r and the tunnelling time t_t. The left part of the figure corresponds to short trajectories and the right part to long trajectories.
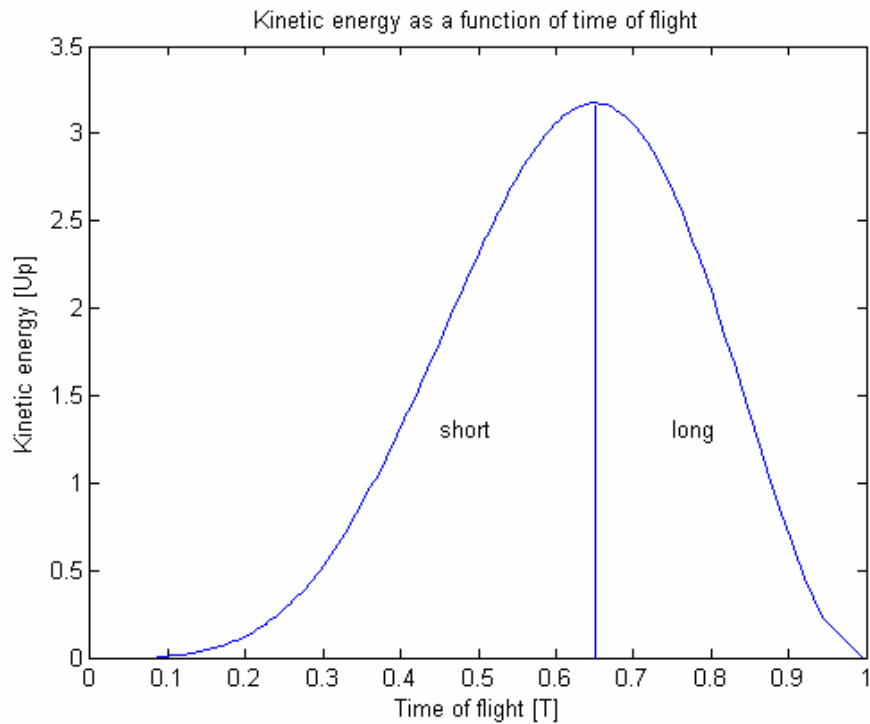
Figure 4.5: Kinetic energy of returning electrons in units of U_p as a function of time of flight, τ, expressed in units of the laser period T.

The maximum energy corresponds to a time of flight τ ≈ 0.65 T. For energies lower than the maximum it is clearly seen that there always exist two electron trajectories that will result in identical relative velocities at the moment of collision, and hence in identical kinetic and photon energies. Each harmonic in the plateau region of the spectrum can

thus be generated by either of these two trajectories, known as the two main quantum paths [5].

The resulting harmonic spectra usually have similar appearances: The first few (low) orders show rapidly decreasing intensities, then the so called plateau region begins with harmonics of about the same yield. Finally, at the cut-off frequency, the harmonic intensities start to fall off again, see figure 4.6.
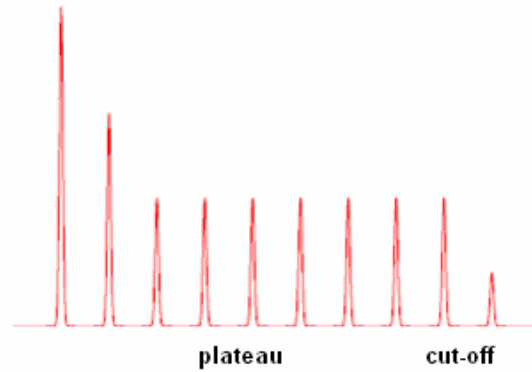

Figure 4.6: Schematic picture of harmonic spectrum.

This appearance is the result of polarisation and the quantum mechanical tunnelling probability. For lower orders, in the perturbative regime, the applied electric field is small compared to the interatomic fields. Then the polarisation P can be expanded in a Taylor series about the electric field $E = 0$ [1], see equation 4.2.

$$P = a_1 E + \frac{1}{2}a_2 E^2 + \frac{1}{6}a_3 E^3 + ... \qquad (4.2)$$

This explains the rapidly decreasing intensities of the low orders. In the strong-field regime the higher order harmonics forming the plateau are generated. Their uniform intensities are explained by a dependence on probability amplitudes for tunnel ionisation, propagation in the laser field and recombination [5] rather than on harmonic order.

4.1.2 The Strong field approximation

However, the classical theory has some limitations. Studying an experimental spectrum it is obvious that the photons are not emitted with continuous energy, but at odd multiples of the fundamental frequency. It also lacks an explanation of the behaviour of the intensity of the harmonics. An improved theoretical description based on quantum mechanics is the so called Strong Field Approximation, SFA.

The electric field of the light incident on the atom displaces the electron cloud relative to the nucleus inducing a nonlinear dipole moment on the atom. The resulting electron dynamics then described by the time dependent Schrödinger equation is very difficult to calculate and three assumptions are made [9,10]:

1. The atom is sufficiently described by one bound state, the ground state, neglecting contributions from all other bound states. Resonant interactions between bound states must be avoided, so that I_p must be much larger than the photon energy of the driving laser field.

$$I_p \gg \hbar\omega$$

2. Depletion of the ground state is neglected, assuming weak ionisation. This requires that $U_p < U_{sat}$.

3. The electron can be treated as a free particle in the continuum, moving in the electric field without being affected by the atomic potential.

Using the strong field approximation the single atom response can be calculated with a method called the saddle point approximation (SPA), and then the nonlinear dipole moment is obtained according to equation 4.3 [11], here in atomic units.

$$x(t) = i\int_{-\infty}^{t} dt' \int d^3p \, E(t') d_x^*[p-A(t)] d_x[p-A(t')] \times e^{-iS(p,t,t')} + \text{c.c} \tag{4.3}$$

E(t) is the electric field of the laser pulse and linearly polarised in the x-direction, *A(t)* is the vector potential of the electric field, *p* is the canonical momentum given by equation 4.4 [10], d_x is the dipole matrix element for bound-free transitions and *S(p,t$_r$,t$_t$)* is the quasi-classical action given by equation 4.5. In equation 4.4 *v* is the kinetic momentum of the outgoing electron.

$$p(t) = v + A(t) \tag{4.4}$$

$$S(p,t_r,t_t) = \int_{t_t}^{t_r} dt\left(\frac{p^2(t)}{2} + I_p\right) \tag{4.5}$$

These calculations give very accurate results for the amplitude and phase of the different harmonic orders. For this project nonadiabatic SPA calculations of harmonic spectra in neon at laser intensities between $5 \cdot 10^{13}$ W/cm^2 and $1 \cdot 10^{15}$ W/cm^2 are performed by Katalin Varjú at University of Szeged in Hungary. Figure 4.7 shows her calculated spectra for laser intensities 3.7-$4.0 \cdot 10^{18}$ W/m^2. These are used for comparison with our experimental results in section 4.4.
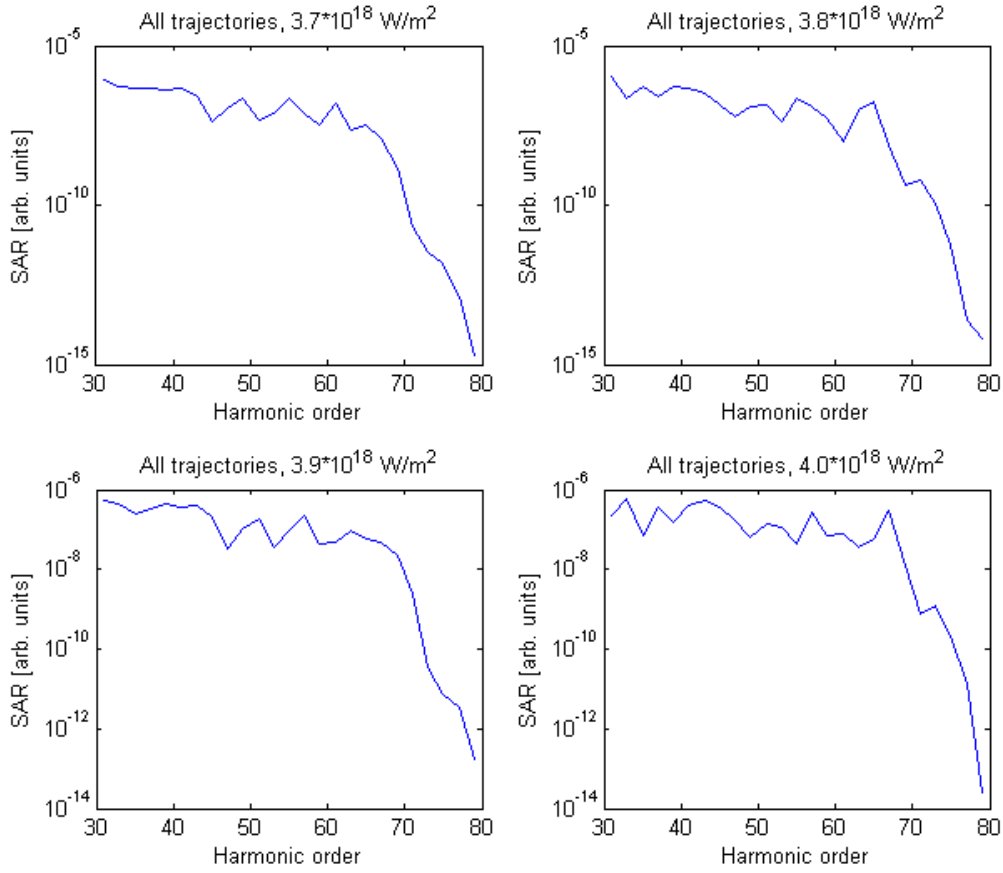
Figure 4.7: Single atom response for intensities 3.7-4.0·10¹⁸ W/m² calculated by Katalin Varjú.

4.1.3 The Single atom phase

The phase of the harmonic radiation with respect to the fundamental laser field can also be calculated in a semi-classical way [14]. The electric field is then simply described as in section 4.1.1 when calculating the classical trajectories with only one force acting upon the electron. The canonical momentum is approximated with the classical electron momentum. The single atom phase is then calculated with equation 4.6, and it appears to depend almost linearly on the laser intensity with a coefficient α.

$$\varphi_{atom} = \frac{S(p,t_t,t_r)}{\hbar} + q\varphi(\rho,z) \approx \alpha I \tag{4.6}$$

Figure 4.8 shows the intensity variation of the single atom phase of harmonic 55 as a function of intensity. The phase of the short trajectories varies much slower than the phase of the long trajectories.
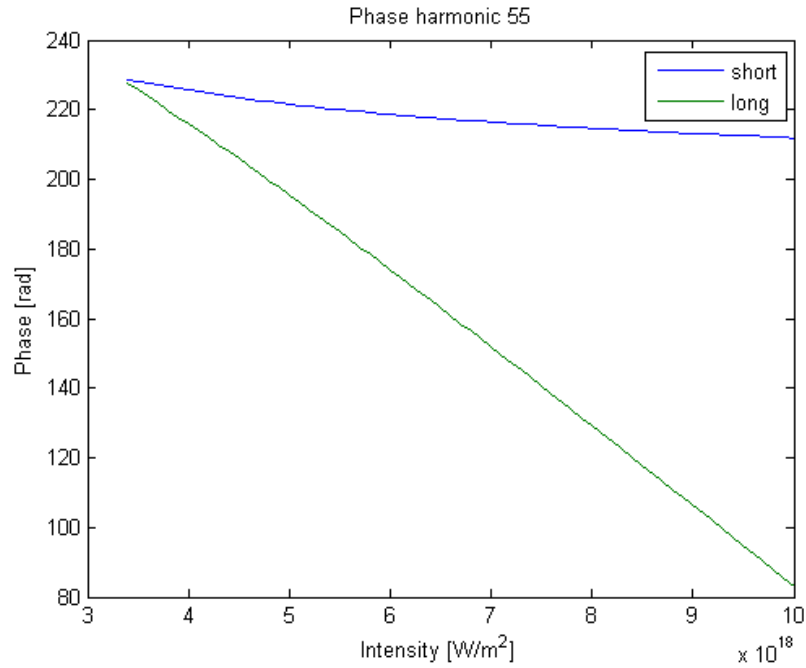
Figure 4.8: Phase of harmonic 55 as a function of laser intensity.

The α coefficients for the harmonic orders observed in the experiments are calculated and the result is displayed in figure 4.9, this is used for the phase matching calculations in section 4.3.
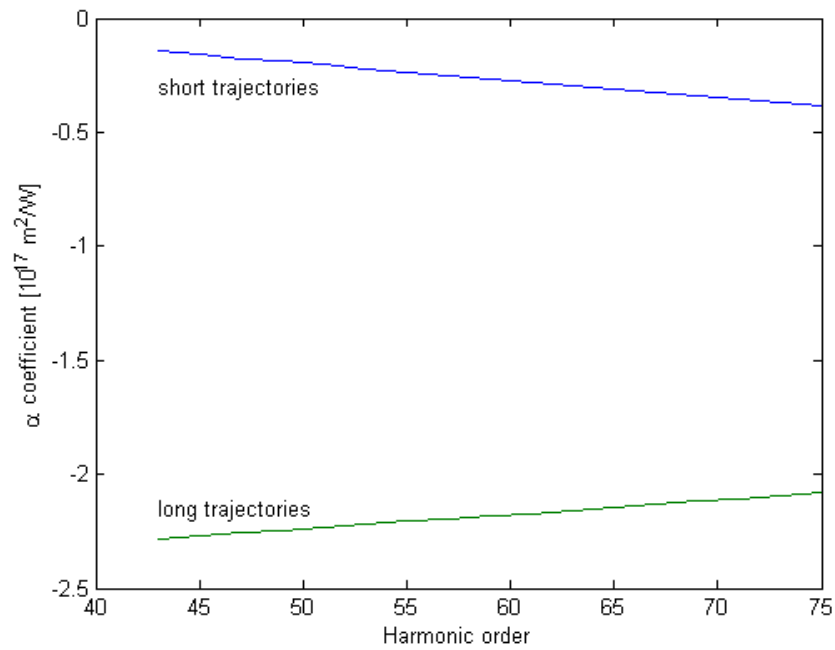

Figure 4.9: α coefficient for harmonic orders 43-75, short and long trajectories.

4.1.4 Ionisation rate

Depending on the laser intensity a certain part of the atoms in the medium will be ionised giving rise to different ionisation rates $r(I_0)$. The free electrons introduce a change in the refractive index of the medium affecting which region of the spectrum that will be phase matched. Phase matching will be discussed in section 4.3 The ionisation rates are determined by first calculating the ionisation probabilities P_{ADK} for different intensities according to the method of instantaneous tunnel ionisation [12], but since this gives rise to too high ionisation probabilities for high laser intensities they have to be corrected with a factor $\beta(I_0)$ according to [13]. The ionisation rates $r(I_0)$ are thus calculated according to equation 4.7 where τ is the laser pulse length, here set to 35 fs in accordance with the laser used in the experimental setup.

$$r = \beta(I_0)P_{ADK}\tau \tag{4.7}$$

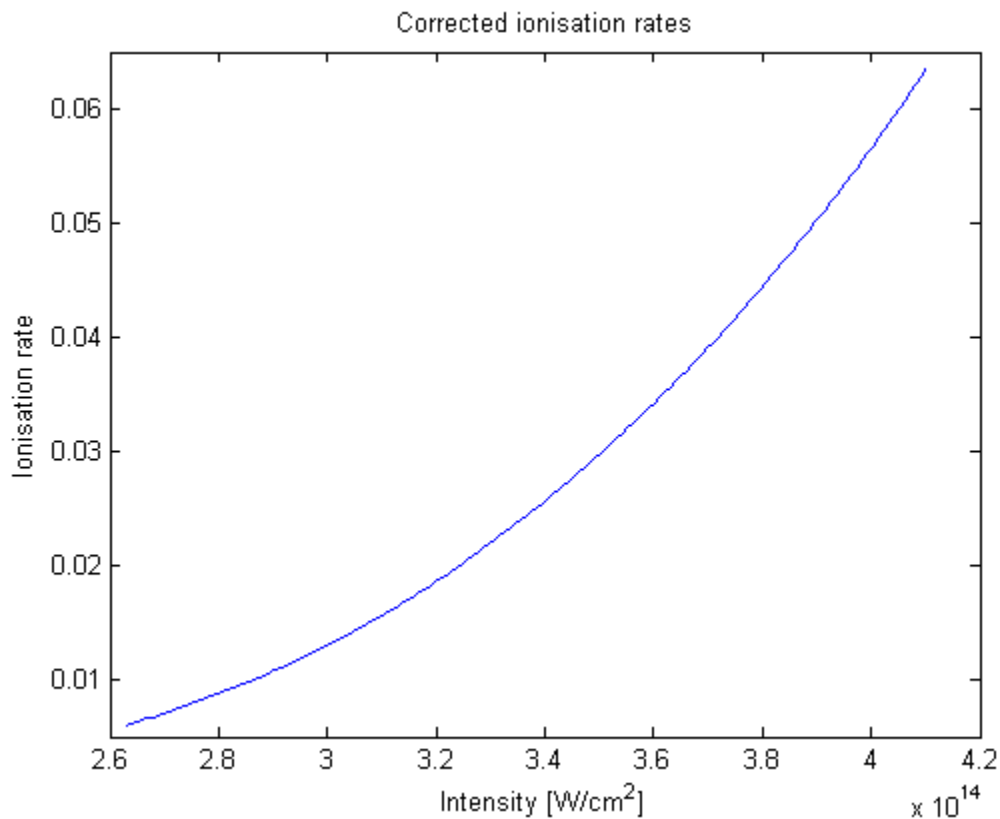In figure 4.10 the corrected ionisation rates are displayed as a function of laser intensity.

Figure 4.10: Corrected ionisation rates as a function of laser intensity.

4.2 *Variation of the single atom response in the medium*

In the previous section the dependence of the single atom phase on the laser intensity was described. Here we look at phase variations of the polarisation in the medium which are exceedingly important for phase matching which is further described in section 4.3. The total macroscopic field is a coherent sum of the radiation generated in each point in the medium, and here the phase variation of the harmonics is an important factor. We also describe the ionisation rate in the medium.

4.2.1 Gaussian beam

The laser beam and the generated harmonic beam both have a Gaussian beam profile. The phase of the generated harmonics is therefore a combination of the phase of a Gaussian beam and the single atom phase described in section 4.1.3. Equations 4.8 and 4.9 [1] describe the intensity variation along the z-axis and the axial and radial (ρ) phase variation of a Gaussian beam, respectively

$$I(0,z) = \frac{I_0}{1 + (z/z_0)^2} \tag{4.8}$$

$$\varphi(\rho,z) = kz - \varsigma(z) + \frac{k\rho^2}{2R(z)} \tag{4.9}$$

In equation 4.8 z_0 is the Rayleigh range. The first term in 4.9, kz, is the phase of a plane wave with wave number k. The second term $\varsigma(z)$ defined in equation 4.10 represents a phase retardation corresponding to a delay of the wave front relative to a plane or spherical wave.

$$\varsigma(z) = \tan^{-1}\left(\frac{z}{z_0}\right) \tag{4.10}$$

As the wave propagates from $z = -\infty$ to $z = +\infty$ the total retardation is π, this is called the *Gouy effect*. The third term describes wave front bending, the phase deviation of an off-axis point (z,ρ) from a point $(z,0)$ on the z-axis. ρ is the radial distance from the z-axis and $R(z)$ is the wave front radius of curvature defined by equation 4.11.

$$R(z) = z\left[1 + \left(\frac{z}{z_0}\right)^2\right] \tag{4.11}$$

The top part of figure 4.11 shows the beam radius and the bottom part shows the wave front radius of curvature.
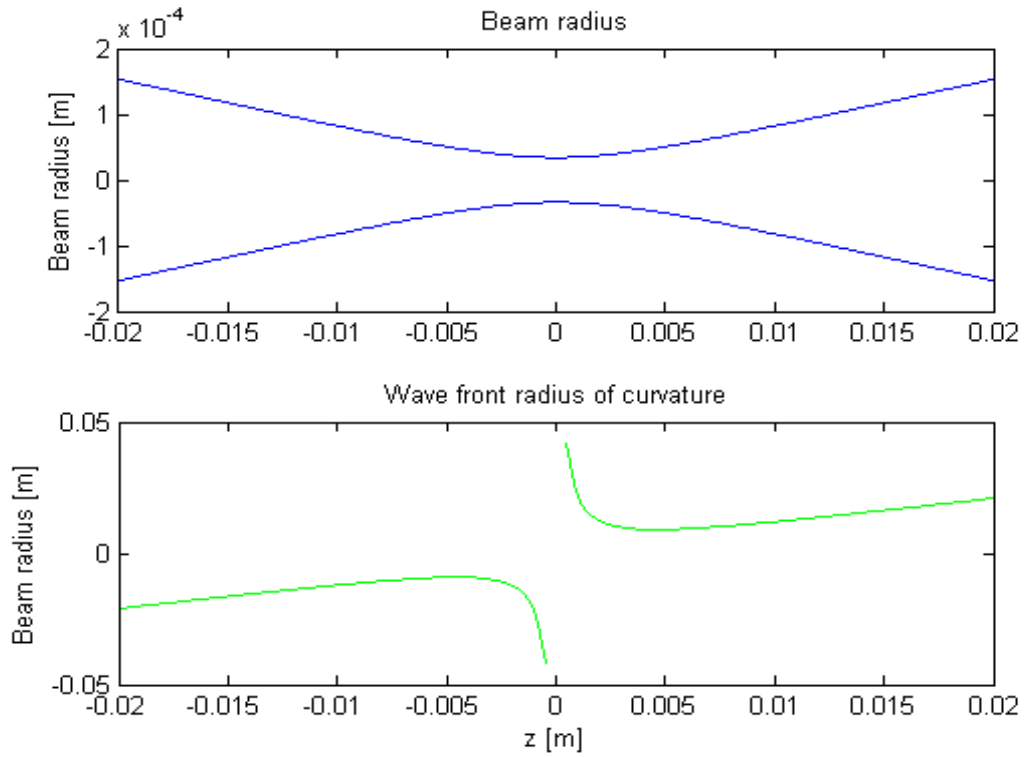
Figure 4.11: *Top:* Longitudinal variation of the radius of a Gaussian beam.
Bottom: Longitudinal variation of the radius of curvature of a Gaussian beam.

Figure 4.12 shows the intensity distribution of a Gaussian beam with $I_0 = 5 \cdot 10^{18} \ \mathrm{W/m^2}$.
In figure 4.13 the total phase of a Gaussian beam according to equation 4.9 is plotted for
the same intensity.

Figure 4.12: Intensity distribution of a Gaussian beam with $I_0 = 5 \cdot 10^{18} \ \mathrm{W/m^2}$.

40

Figure 4.13: Phase of a Gaussian beam with $I_0 = 5 \cdot 10^{18}\ \mathrm{W/m^2}$.
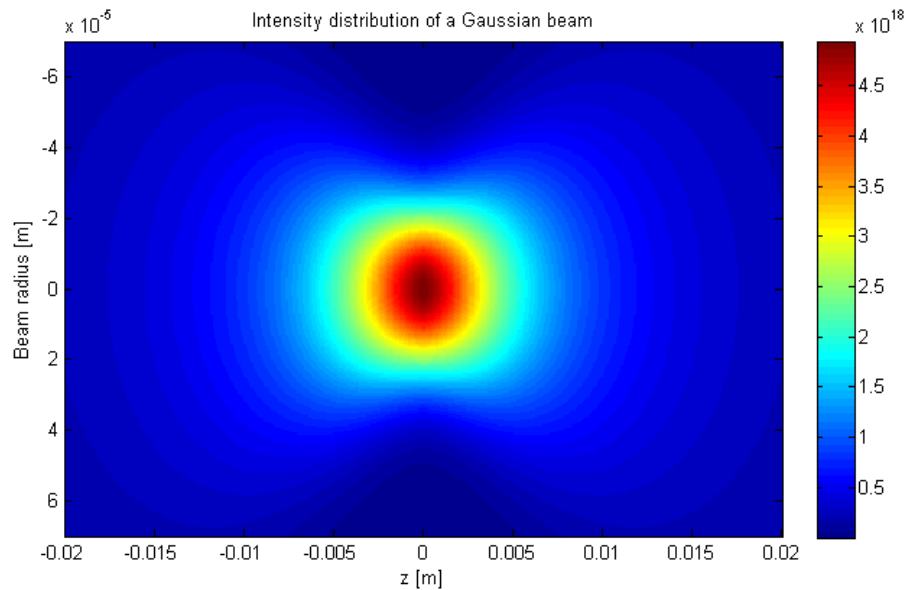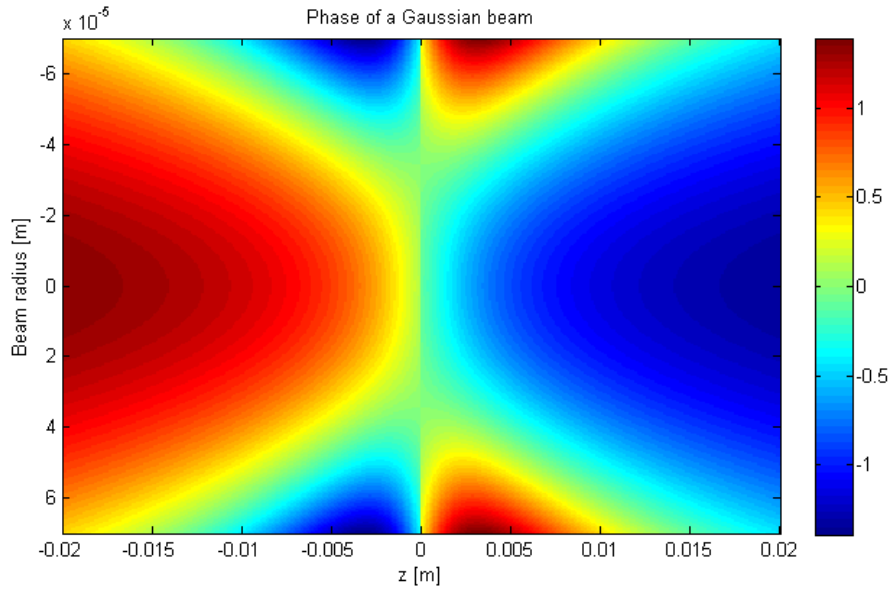
4.2.2 Phase variation of the polarisation in the medium

As shown in figure 4.13 the phase of the Gaussian beam is varying quite slowly, but as mentioned before the harmonic phase is a superposition of the Gaussian and the single atom phase. Figures 4.14 and 4.15 show the single atom phase and the total phase of the 65:th harmonic in a longitudinal cross section of the beam plotted modulus 2π. The left parts of the figures display the phase of a long trajectory and the right parts show the phase of a short trajectory. Comparing figures 4.13 and 4.15 the importance of the single atom phase becomes evident. Here as well as in figure 4.8 it is obvious that the phase of the short trajectory varies much slower than the phase of the long trajectory leaving a larger region suitable for phase matching.
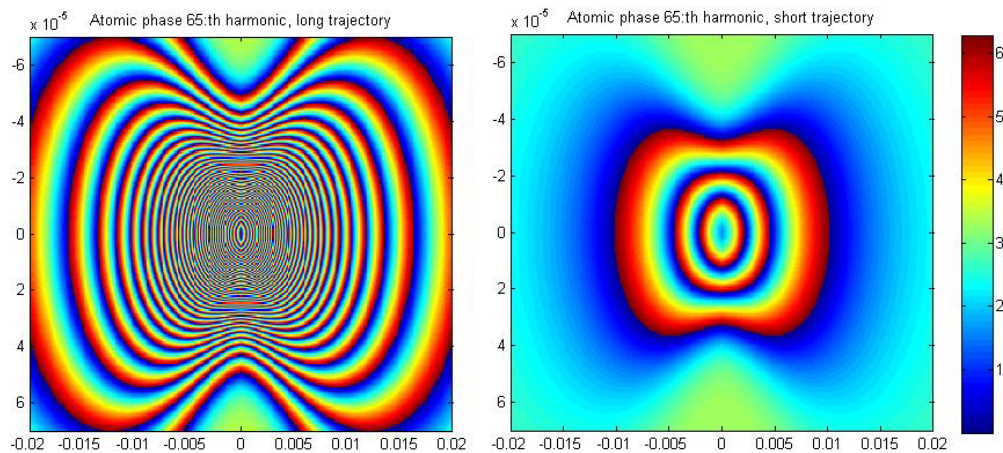
Figure 4.14: Single atom phase plotted modulus 2π. *Left*: Long trajectory and *right*: Short trajectory.
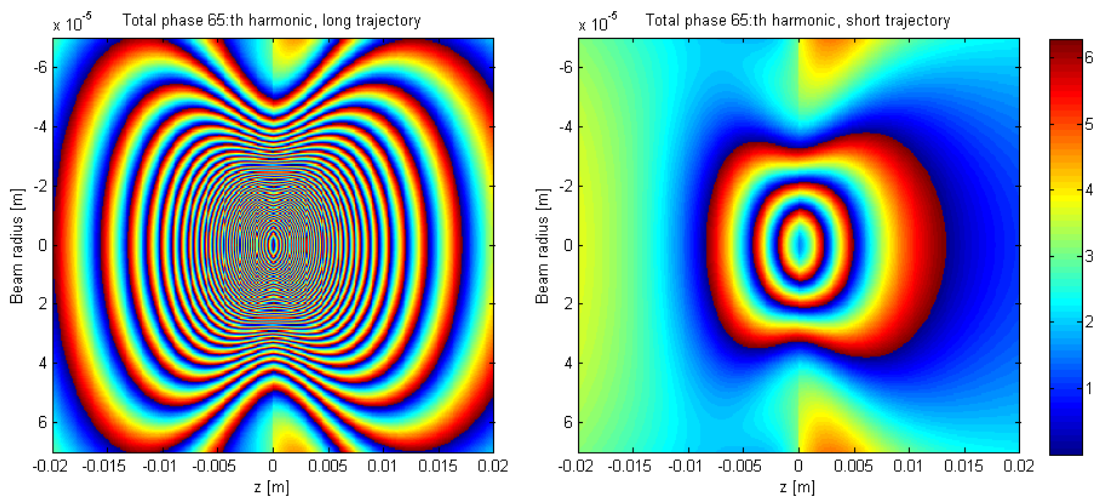
Figure 4.15: Total phase plotted modulus 2π. *Left*: Long trajectory and *right*: Short trajectory.

4.2.3 Ionisation rate in the medium

Due to the intensity variation in the medium the ionisation rate in the medium will also change so that the harmonic generation will be affected depending on where the focus of the laser beam is located relative to the target gas. Figure 4.16 shows the longitudinal variation of the ionisation rate in the medium for a few different values of I_0. As expected the ionisation rate is largest in the focus where the highest intensity is found.

Figure 4.16: Ionisation rate in the medium as a function of intensity and longitudinal position in the beam, the focus is at $z = 0$ m.

4.3 Phase matching

High order harmonic generation HHG is a non-linear optical process in which a strong laser field interacts with atoms in a material, often a gas, and imposes a dipole moment on them. The electric fields generated by the different atoms ad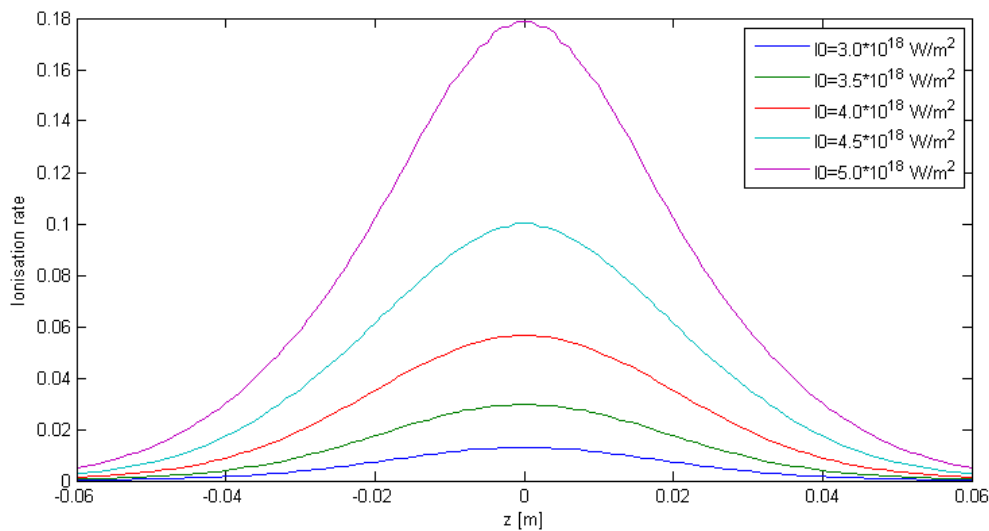d coherently so that the resulting electric field scales as the number density of atoms N, and the harmonic yield scales as N^2 [8]. This argument assumes that all of the atomic dipoles add constructively but whether this is the case or not is known as phase matching. If phase matching is not completely accomplished this simple N^2 dependence may become much more complicated. Only harmonics which are in phase with the fundamental field will result in a signal.

Consider an electric field comprising two harmonic components ω_1 and ω_2, these components may be of different or (as in second harmonic generation) equal frequencies. The nonlinear component of the polarisation then contains components at five frequencies, 0, $2\omega_1$, $2\omega_2$, $\omega_+ = \omega_1 + \omega_2$ and $\omega_- = \omega_1 - \omega_2$. All of these waves are not necessarily generated since certain phase matching conditions must be satisfied. This can be illustrated by letting waves 1 and 2 be plane waves with wavevectors $\mathbf{k}_1$ and $\mathbf{k}_2$. The medium can then act as a light source of frequency $\omega_3 = \omega_1 + \omega_2$ if the frequency matching condition in equation 4.12 and the phase matching condition in equation 4.13 is met [1]. A small phase mismatch $\Delta\mathbf{k} = \mathbf{k}_3 - \mathbf{k}_1 - \mathbf{k}_2 \neq 0$ may result in a considerable reduction in the wave-mixing efficiency.

$$\omega_1 + \omega_2 = \omega_3 \tag{4.12}$$

$$\mathbf{k}_1 + \mathbf{k}_2 = \mathbf{k}_3 \tag{4.13}$$

Phase matching in HHG can be studied theoretically in one dimension by numerically calculating a phase matching coefficient, as has been done by T. Ruchon et al [15]. The phase matching coefficient is expressed by equation 4.14.

$$F_q = e^{-i\langle\Phi_q\rangle} e^{-\kappa_q L/2} \frac{e^{(i\Delta k_q + \kappa_q)L/2} - e^{(-i\Delta k_q - \kappa_q)L/2}}{i\Delta k_q + \kappa_q} \tag{4.14}$$

L is the length of the medium, $\langle\varphi_q\rangle$ is an average phase for the qth harmonic, Δk_q is the phase mismatch (i.e. the difference between the imaginary parts of the wave vectors for harmonic q and the fundamental) and κ_q is the absorption of the qth harmonic. In the absorption limit, for long media, $e^{-\kappa_q\frac{L}{2}} \approx 0$. The phase factor can thus be omitted and only the modulus is calculated resulting in equation 4.15.

$$|F_q| = \frac{1}{\sqrt{\Delta k_q^2 + \kappa_q^2}} \tag{4.15}$$

It is worth mentioning that all of the following equations are in SI units. The phase mismatch Δk_q (equation 4.16) consists of three terms: The first term Δk_{disp} arises from material dispersion (equation 4.17), the second term Δk_{plasma} from plasma dispersion due to free electrons (equation 4.18) and the third term is a contribution from the derivative of the dipole phase Δk_{dipole} (equation 4.19).

$$\Delta k_q = \Delta k_{disp} + \Delta k_{plasma} + \Delta k_{dipole} \tag{4.16}$$

$$\Delta k_{disp} = \left(n_q - n_1 \right) \cdot \frac{q\omega}{c} \tag{4.17}$$

$$\Delta k_{plasma} = \left(n_{pq} - n_{p1} \right) \cdot \frac{q\omega}{c} \tag{4.18}$$

$$\Delta k_{dipole} = \frac{\partial}{\partial z}\left(\frac{\alpha_q I_0}{1 + \frac{z^2}{z_0^2}} \right) \approx \frac{-2\alpha_q I_0 z}{z_0^2} \tag{4.19}$$

In equation 4.17 the refractive index n_1 of the fundamental is calculated from the static polarisability α_{dip} according to equation 4.20 and 4.21 [16]. N_0 is the density of neon atoms and ε_0 is the permittivity of free space.

$$\alpha_{dip} = 2 \cdot 2.67 \, \text{au} \cdot 1.6488 \cdot 10^{-41} = 8.8046 \cdot 10^{-41} \, \frac{\text{Cm}^2}{\text{V}} \tag{4.20}$$

$$n_1 = 1 + N_0 \cdot \frac{\alpha_{dip}}{2\varepsilon_0} \tag{4.21}$$

In 4.18 n_{pq} and n_{p1} are the plasma refractive indices of the harmonics and the fundamental respectively, described by equation 4.22. Here ω_p is the plasma frequency described by equation 4.23, e and m are the electron charge and mass, respectively.

$$n_{pq} = \sqrt{1 - \left(\frac{\omega_p}{q\omega} \right)^2} \tag{4.22}$$

$$\omega_p = \sqrt{\frac{N_e \cdot e^2}{m\varepsilon_0}} \tag{4.23}$$

In equation 4.19 α_q is the same as the α coefficient calculated in the previous section, but here only the short trajectory coefficient is used. The distance between the gas cell and the focus is denoted z and z_0 is the Rayleigh range.

The absorption coefficient κ_q is calculated by multiplying the photoabsorption cross section, σ_{photo}, with the neon density in the gas cell, ρ_{Ne}. See equation 4.24.

$$\kappa_q = \sigma_{photo} \cdot \rho_{Ne} \qquad (4.24)$$

The photoabsorption cross section and n_q values for different wavelengths in neon were taken from the home page of Center for X-Ray Optics at Lawrence Berkeley National Laboratory [17].

An important parameter is the ionisation rate $r(I_0)$ since the free electron density depends on it, and thereby many other parameters. The ionisation rates are calculated as described in section 4.1.3. The modulus of F_q is calculated for a few different values of z and r. Figures 4.17 and 4.18 show $\left| F_q \right|$ at a few different ionisation rates, the first with the gas cell situated 1 cm before the focus and the second 3 cm after the focus. An interesting conclusion is that with the gas cell placed before the focus the phase matched region moves from high to low orders with increasing ionisation rate while the opposite happens when the gas cell is placed after the focus. Another conclusion is that a higher ionisation rate is needed after the focus than before to phase match the same part of the spectrum.
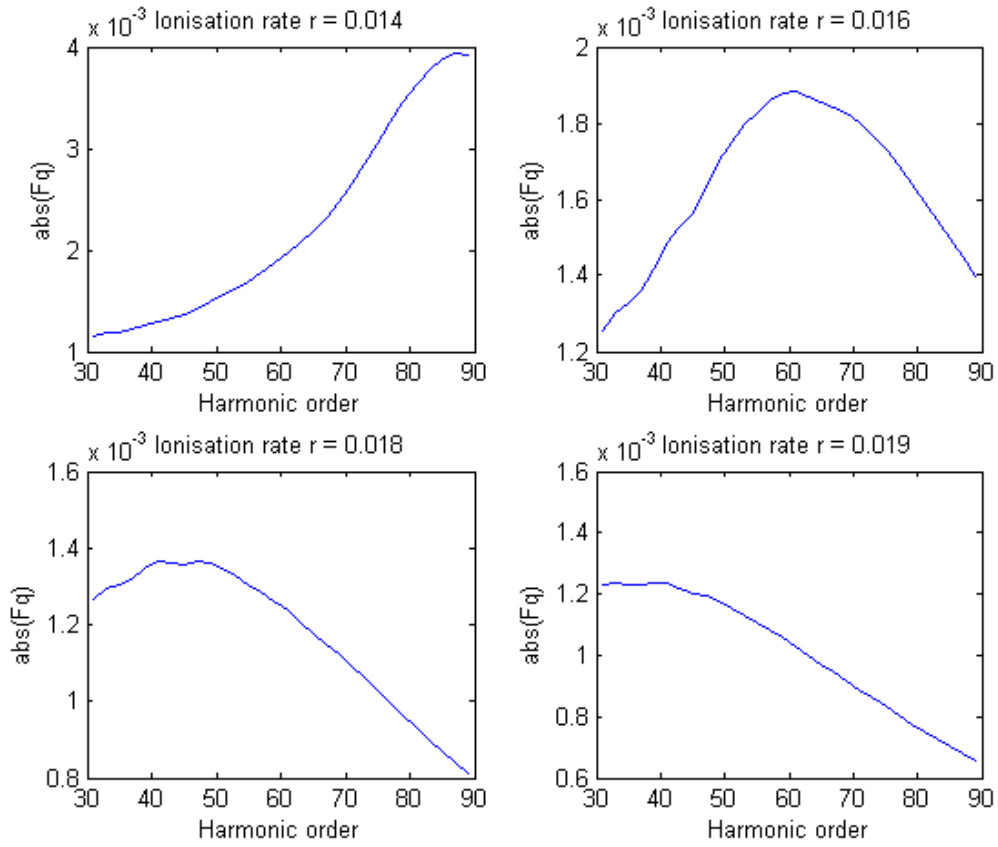
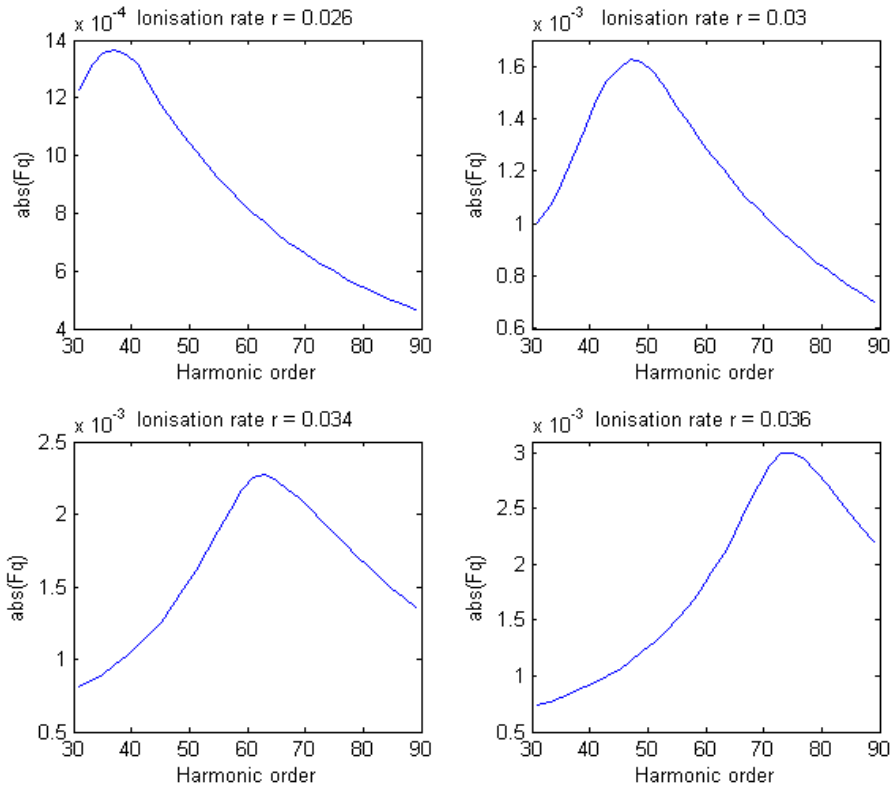**Figure 4.17:** $|F_q|$ for four different ionisation rates, $z = -0.01$ m.

Figure 4.18: $|F_q|$ for four different ionisation rates, $z = 0.03$ m.

Finally the modulus of F_q is compared to the corresponding single atom responses calculated by Katalin Varjú, the result is displayed in figure 4.19. The single atom response does not seem to have a significant effect on the phase matched region or the cut off. Before the focus the phase matched region does not even exist according to the single atom response, but after the focus the correspondence is better. These intensities are not very high so the single atom response shows only a slowly rising cut off. The conclusion must still be that phase matching is the most important factor explaining our experimental results.
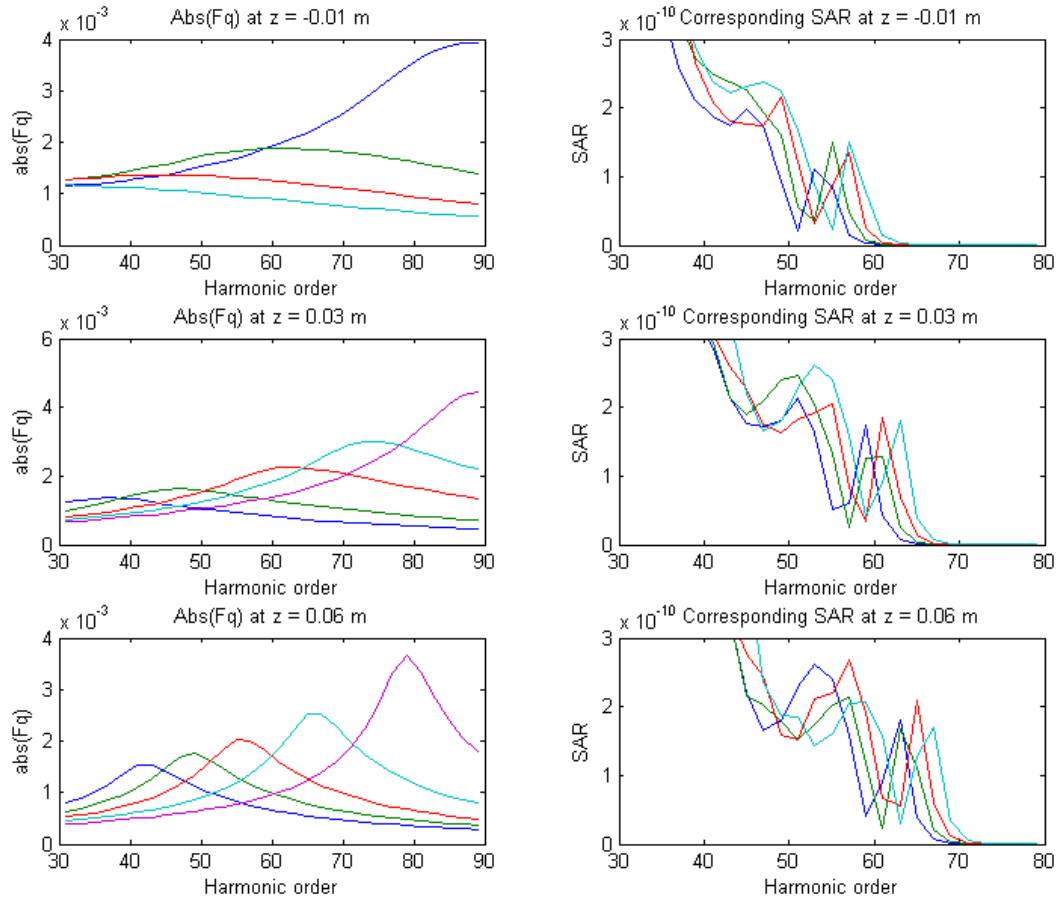
Figure 4.19: Comparison of $|F_q|$ and SAR with the gas cell placed 1 cm before and 3 and 6 cm after the focus. For z = -1 cm the intensities are (dark blue, green, red, light blue) 3.0 - 3.3·10^{18} W/m^2 corresponding to ionisation rates between 0.014 and 0.02. For z = 3 cm I is between 3.4 and 3.7 W/m^2 with r between 0.026 and 0.038. For z = 6 cm I is between 3.7 and 4.1·10^{18} W/m^2 (4.0·10^{18} W/m^2 is the highest value for SAR) with r between 0.04 and 0.06.

4.4 Comparison with experiment

Both experimental spectra and simulated results for the spectrometer with the focus of the harmonic beam located between the VLS grating and the detector show maxima with their ends bent downwards. This implies that the gratings used in the spectrometer actually do focus the signal before the detector. Simulations also prove that if it is possible to move the detector closer to the focus, either by keeping the slit and moving the detector or removing the slit and inserting the harmonic generation in its place, the system resolution may be significantly improved. The latter would also improve the signal strength since much of it is cut by the entrance slit.

Calculations of the single atom phase for different harmonics demonstrates that the short trajectory shows a much slower phase variation than the long trajectory and thus a larger region suitable for phase matching appears so that the short trajectory gives a stronger signal than the long trajectory. The harmonic beam generated by long trajectories also has a larger divergence than the one resulting from short trajectories and this can also be seen in the experimental spectra. The centre part of the spectrum is much brighter than the outer parts as a result of the stronger signal generated by the short trajectories.

Experiments prove that it is indeed possible to reach 100 eV (harmonic order 65) in neon with this setup. Another very interesting result is that we managed to change the phase matching condition so that different parts of the spectrum were enhanced just by varying the iris diameter. According to approximate calculations the intensity in the focus is very high during experiments, up to 10^{19} W/m^2. Comparing with the theoretical cut off law our experimental cut off is much lower, see figure 4.19. Also the ionisation rate would be 1 under these circumstances so the intensity is most likely not that high.
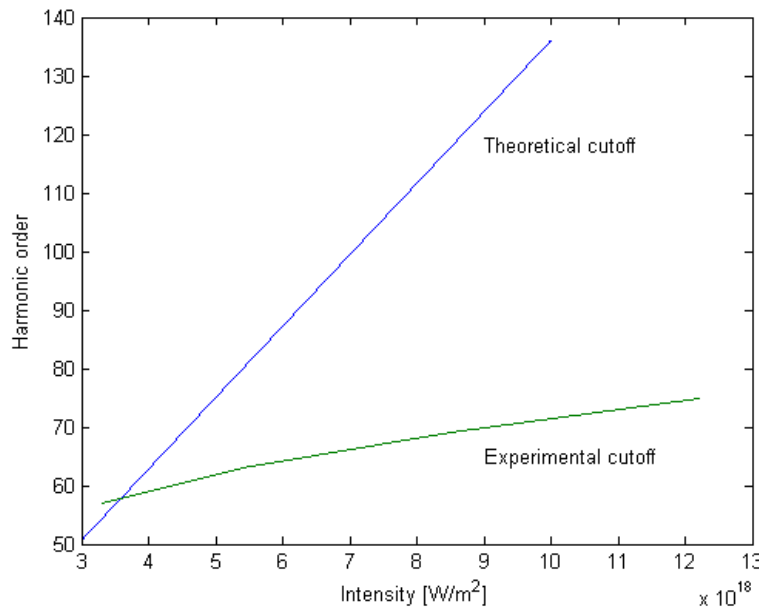

Figure 4.20: Theoretical cut off according to the cut off law and experimental cut off.

Calculations of the phase matching coefficient indicate that when the gas cell is located before the focus the phase matched part of the spectrum moves from higher to lower orders when the ionisation rate grows, which is an unexpected result. Once the gas cell is placed after the focus the phase matched part of the spectrum moves towards higher orders for higher ionisation rates, which is exactly what we saw in the experiments. The calculations also indicate that lower ionisation rates are needed before the focus than after, the further behind the focus the gas cell is positioned the higher ionisation rate and thus intensity needed to phase match a certain part of the spectrum, see figure 4.20. According to the calculations a quite low ionisation rate is needed to phase match the part of the spectrum corresponding to our experimental results which also indicates that the intensity in our experiments is not very high. Comparing our experimental results to Katalin Varjú's calculations of single atom response you can see that for such low intensities those spectra do not change much whereas the phase matching calculations, $|F_q|$, show a large dependence also on small changes in intensity and ionisation rate. Looking at the single atom response the cut off does not change significantly at low intensities, which indicates that phase matching is a more important factor than single atom response.
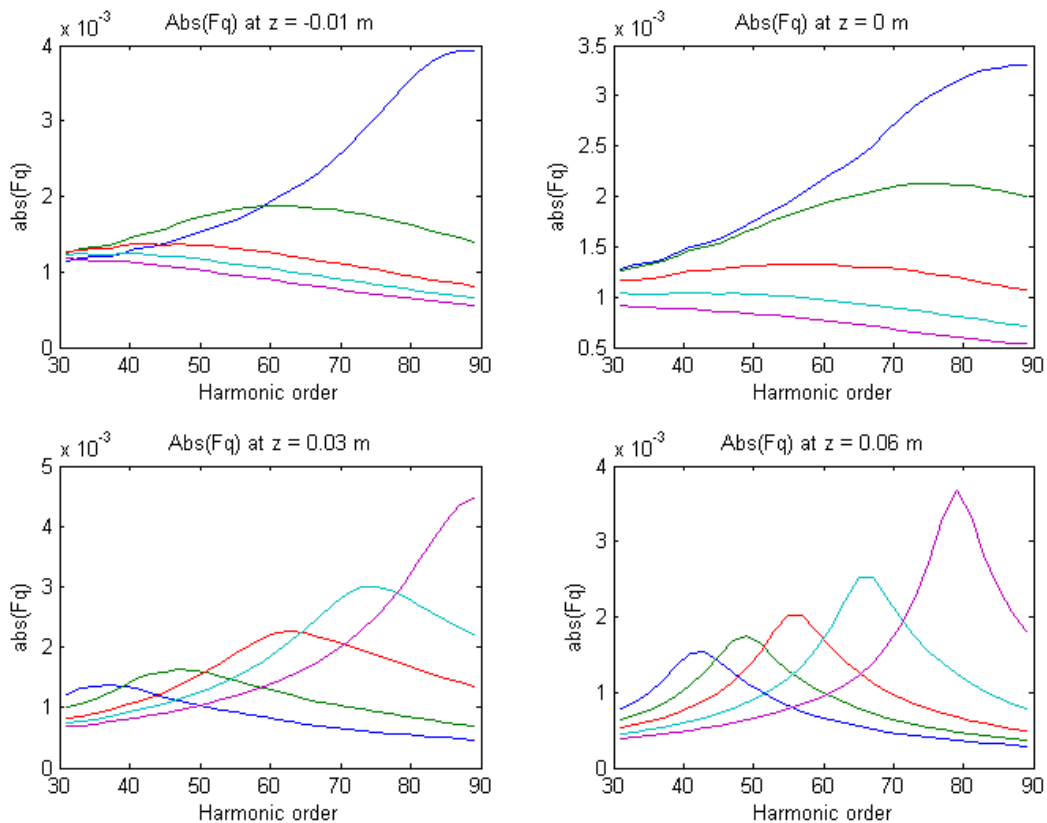

Figure 4.21: $|F_q|$ calculated for different values of *I*, *r* and z. In the diagram for z = -0.01 m the intensity *I* is between 3.04 and 3.24·10^{18} W/m^2, r is 0.014-0.02. In the next diagram showing the focus (z = 0 m) *I* is 3.21-3.41·10^{18} W/m^2 with *r* between 0.019 and 0.026. The third diagram shows z = 0.03 m, *I* is 3.41-3.68·10^{18} W/m^2 and *r* is between 0.026 and 0.038 and the last diagram shows z = 0.06 m with *I* between 3.72 and 4.05·10^{18} W/m^2, *r* is 0.04-0.06.

5 Summary and outlook

Studying the design of the XUV flat field spectrometer through FRED simulations I learned many interesting things about the imaging properties of the system and the focusing properties of a varied line-space grating. It was discovered that the curvature observed in the experimental spectra is a result of the curvature of the toroidal mirror and the focus of the harmonics being located between the VLS grating and the detector. Simulations also showed that the new aluminium plate blocking the fundamental was installed in a good position far from the fundamental focus with no risk of blocking the signal. The modified spectrometer was tested in experiments with argon as target gas and it was decided that the new optics could be safely installed before beginning experiments with neon. With the new optics installed the signal proved to be enhanced, mainly due to the now much lower background.

During the neon experiments it was discovered that the signal is much more dependent on correct alignment in neon than in argon, much due to the long gas cell needed. Once a signal was obtained it proved to contain harmonics well into the 100 eV range that we aimed for. Another interesting discovery was that just by altering the diameter of the iris cutting part of the beam different parts of the spectrum became visible. This was assumed to be a result of changes in the phase matching condition due to variation of the laser intensity in the medium and thereby also altering of the ionisation rate. This assumption was then supported by numerical phase matching calculations in one dimension.

The new insights into the spectrometer design can be used for further modifications, for example improving the resolution and signal strength, or even designing a new spectrometer. It may also be useful when deciding on which grating is best suited for a certain experiment. The phase matching calculations performed here show very interesting results, but it is a simple model that needs to be confirmed by more thorough calculations and a better model.

Finally I want to say that I particularly appreciate the versatile nature of this project. I got to investigate the design of an instrument used in experiments, I had practical training during experiments as well as gained a deeper theoretical understanding of the physics of HHG and phase matching. I would like to thank Katalin Varjú for helping me with single atom response calculations and my supervisors, Anne L'Huillier for helping me with the theoretical part and for her valuable comments on my thesis, and Xinkui He for sharing his invaluable insights in experimental procedures and helping me around the lab.

6 References

1. Bahaa E.A. Saleh, Malvin Carl Teich, "Fundamentals of Photonics", John Wiley & Sons inc. (1991)

2. E. Georgiadou, "Study of harmonic generation with a two-color field", Lund Reports on Atomic Physics, LRAP-375 (2007)

3. L. Garifo, A. M. Malvezzi, and G. Tondello, "Grazing incidence spectrograph-monochromator with a focusing toroidal mirror", APPLIED OPTICS, Vol. 18, No. 12, 15 June 1979

4. Christopher Palmer, "Diffraction grating handbook", Thermo RGL (2002)

5. Thomas Brabec, Ferenc Krausz, "Intense few-cycle laser fields: Frontiers of nonlinear optics", Review of Modern Physics, Vol. 72, No. 2 (2000)

6. Christoph Heyl, "High Order Harmonic Generation with Two Color Laser Fields", Lund 2008

7. F. Geier, "Optimization of High-Order Harmonic Generation", Lund university, LRAP-386 (2007)

8. P. Balcou et al: High-order-harmonic generation: towards laser-induced phase-matching control and relativistic effects. Appl. Phys. B, 74, 509–515 (2002)

9. M. Dahlström, "Strong Field Approximation for High Order Harmonic Generation with $\omega/2\omega$ Laser Fields", Lund Reports on Atomic Physics, LRAP-381 (2007)

10. M. Lewenstein, Ph. Balcou, M. Yu. Ivanov, A. L'Huillier, P. B. Corkum, "Theory of high-harmonic generation by low frequency laser fields", Phys. Rev. A, 49, 3 (1994)

11. G. Sansone, C. Vozzi, S. Stagira, M. Nisoli, "Nonadiabatic quantum path analysis of high-order harmonic generation: Role of the carrier envelope phase on short and long paths", Phys. Rev. A, 70, 013411 (2004)

12. M. V. Ammosov, N. B. Delone, V. P. Krainov, "Tunnel ionization of complex atoms and of atomic ions in an alternating electromagnetic field", Zh. Eksp. Teor. Fiz. **91**, 2008 (1986) [Sov. Phys. JETP **64**, 1191 (1986)]

13. M. B. Gaarde, M. Murakami, R. Kienberger, "Spatial separation of large dynamical blueshift and harmonic generation", Phys. Rev. A, 74, 053401 (2006)

14. F. Linder, W. Stremme, M.G. Schätzel, F. Grasbon, G.G. Paulus, H.Walther, R. Hartmann, L. Strüder, "High-order harmonic generation at a repetition rate of 100 kHz", Phys. Rev. A, 68, 013814 (2003)

15. T. Ruchon, C. P. Hauri, K. Varjù, E. Mansten, M. Swoboda, R. López-Martens, A. L'Huillier, "Macroscopic effects in attosecond pulse generation", New Journal of Physics 10 (2008)

16. P. Soldán, E. P. F. Lee, T. G. Wright, "Static dipole polarizabilities (α) and static second hyperpolarizabilities (γ) of the rare gas atoms (He-Rn)", Phys. Chem. Chem. Phys., 2001, 3, 4661-4666

17. Retrieved from http://henke.lbl.gov/optical_constants/ 2008-12-19